Intermittency at Earth's bow shock: Measures of turbulence in quasi-parallel and quasi-perpendicular shocks

James Plank[1] and Imogen Gingell[2]

[1]University of Southampton
[2]Imperial College London

March 7, 2023

Abstract

Turbulent plasmas such as the solar wind and magnetosheath exhibit an energy cascade which is present across a broad range of scales, from the stirring scale at which energy is injected, down to the smallest scales where energy is dissipated through processes such as reconnection and wave-particle interactions. Recent observations of Earth's bow shock reveal a disordered or turbulent transition region which exhibits features of turbulent dissipation, such as reconnecting current sheets. We have used observations from Magnetospheric Multiscale (MMS) over four separate bow shock crossings of varying ϑ_{Bn} to characterise turbulence in the shock transition region and how it evolves towards the magnetosheath. We observe the magnetic spectrum evolving by fitting power laws over many short intervals and find that the power-law index in the shock transition region is separable from that of the upstream and downstream plasma, for both quasi-perpendicular and quasi-parallel shocks. Across the shock, we see a change in the breakpoint location between inertial and ion power-law slopes. We also observe the evolution of scale-independent kurtosis of magnetic fluctuations across the shock, finding a reduction of high kurtosis intervals downstream of the shock, which is more apparent in the quasi-perpendicular case. Finally, we adapt a method for calculating correlation length to include a high-pass filter, allowing estimates for changes in correlation length across Earth's bow shock. In a quasi-perpendicular shock, we find the correlation length to be significantly smaller in the magnetosheath than in the solar wind, however the opposite can occur for quasi-parallel shocks.

Intermittency at Earth's Bow Shock: Measures of Turbulence in Quasi-Parallel and Quasi-Perpendicular Shocks

J. Plank[1], **I. L. Gingell**[1]

[1]School of Physics & Astronomy, University of Southampton, Southampton, UK

Key Points:

- We examine the evolution of turbulent fluctuations across Earth's bow shock using magnetic spectra, kurtosis and correlation length.
- The power-law magnetic spectra in the shock transition region are found to be distinct from the solar wind and magnetosheath.
- The correlation length of high-pass filtered fluctuations shows fast reduction of the driving scale across a quasi-perpendicular shock.

Corresponding author: James Plank, `jp5g16@soton.ac.uk`

Abstract

Turbulent plasmas such as the solar wind and magnetosheath exhibit an energy cascade which is present across a broad range of scales, from the stirring scale at which energy is injected, down to the smallest scales where energy is dissipated through processes such as reconnection and wave-particle interactions. Recent observations of Earth's bow shock reveal a disordered or turbulent transition region which exhibits features of turbulent dissipation, such as reconnecting current sheets. We have used observations from Magnetospheric Multiscale (MMS) over four separate bow shock crossings of varying θ_{Bn} to characterise turbulence in the shock transition region and how it evolves towards the magnetosheath. We observe the magnetic spectrum evolving by fitting power laws over many short intervals and find that the power-law index in the shock transition region is separable from that of the upstream and downstream plasma, for both quasi-perpendicular and quasi-parallel shocks. Across the shock, we see a change in the breakpoint location between inertial and ion power-law slopes. We also observe the evolution of scale-independent kurtosis of magnetic fluctuations across the shock, finding a reduction of high kurtosis intervals downstream of the shock, which is more apparent in the quasi-perpendicular case. Finally, we adapt a method for calculating correlation length to include a high-pass filter, allowing estimates for changes in correlation length across Earth's bow shock. In a quasi-perpendicular shock, we find the correlation length to be significantly smaller in the magnetosheath than in the solar wind, however the opposite can occur for quasi-parallel shocks.

Plain Language Summary

Turbulence is a phenomenon that can arise in anything that behaves like a fluid under certain conditions. The size and shape of turbulent vortices and eddies can tell us a lot about the energy contained within the fluid. For example, highly energetic particles emitted from the Sun form a turbulent, fluid-like plasma called the solar wind. The Earth's magnetic field acts as an obstacle to the solar wind, forming a shock wave called the bow shock, similar to the shock wave formed by a supersonic jet in air. This shock wave is very complex and introduces an additional source of turbulent structures. In this paper, we looked at the turbulence just before the shock wave, during, and after to learn if its presence fundamentally changes how the energy gets distributed inside a turbulent plasma. We found evidence that turbulence behaves differently in these three areas. In addition, the magnetic field angle relative to the shock wave (i.e. nearly parallel/perpendicular to the shock) also has an effect.

1 Introduction

Turbulence is a ubiquitous phenomenon in space plasmas, occurring in systems ranging from star formation (McKee & Ostriker, 2007) to galaxy clusters (Zhuravleva et al., 2014) to planetary magnetospheres (Chasapis et al., 2018) and the solar wind (Alexandrova et al., 2013; Bruno & Carbone, 2013; Kiyani et al., 2015). In collisionless plasmas such as the solar wind, the mechanisms for dissipating energy in turbulence are not well-known (Kiyani et al., 2015), and solving this problem is vital for our understanding of turbulence in general. In the heliosphere, for example, turbulent dissipation is a suggested source of the heating observed in the Solar corona (Cranmer et al., 2015; Klimchuk, 2006). One of several proposed solutions to this dissipation problem is magnetic reconnection (Carbone et al., 1990; Franci et al., 2017), in which local changes in magnetic topology rapidly transfer energy from fields to particles, resulting in particle acceleration and heating (Burch et al., 2016). Some other possible explanations for energy dissipation include wave-particle interactions, driven by cyclotron resonance or kinetic Alfvén waves (Isenberg & Hollweg, 1983; Hollweg, 1999).

One advantage of using the local space environment to study plasma turbulence is that it allows for high-cadence in-situ observation of structures associated with turbulent dissipation, such as reconnecting current sheets. The Magnetospheric Multiscale (MMS) mission has recently been used to observe electron outflow jets at thin current sheets - a signature of reconnection - in Earth's magnetosheath (Phan et al., 2018) and the bow shock transition region (Gingell et al., 2019; Wang et al., 2017). Recent simulations (Bessho et al., 2020, 2022; Gingell et al., 2017; Matsumoto et al., 2015) have shown that processes in the shock foot can generate current sheets and magnetic islands, contributing to the formation of a transition region that can appear turbulent. The properties of turbulence are also known to vary across different plasma regimes, such as the solar wind and magnetosheath (Alexandrova, 2008). Furthermore, the properties of turbulence are also known to vary within the magnetosheath, varying with the upstream shock orientation (Yordanova et al., 2020) and between the sub-solar point and flanks (Huang et al., 2017; Sahraoui et al., 2020). Hence, these observations of turbulence and coherent structures in the shock layer, and differences in the character of turbulence throughout the magnetosheath together raise two open questions: 1) Is there a measurable difference between turbulence seen in the bow shock transition region and in the surrounding plasma (i.e. the solar wind and magnetosheath)? And 2) How quickly does well developed turbulence arise in the magnetosheath after a bow shock crossing? For both of these questions we also compare the differences between quasi-parallel and quasi-perpendicular shocks.

We note that some definitions of turbulence require a 'well-developed' inertial range, allowing a complete cascade from the largest, fluid-like scales in the plasma, through the kinetic regime and ending at the dissipation scale. In the shock transition region, disordered fluctuations may be driven by non-linear interactions and instabilities that arise at scales smaller than the inertial range, but nevertheless appear to cascade and dissipate energy in the region. In this study we will refer to these processes as turbulent, however it is possible that they will not always fit the definition of fully developed turbulence.

In this paper, we address the above observations by studying the evolution of magnetic fluctuations from the solar wind to magnetosheath, i.e. across the bow shock, using three different measures of turbulence: the magnetic spectrum, the kurtosis, and the correlation length (e.g. Stawarz et al., 2019). From the magnetic spectrum we extract the spectral break between inertial and ion scale ranges, which is related to local plasma scales such as the ion gyroradius ρ_i, and inertial length d_i (Chen et al., 2014; Franci et al., 2015). We found that the magnetic spectrum in the shock transition region was steeper than both upstream and downstream regions at the electron scale in the quasi-perpendicular event. Observing scale independent kurtosis, we saw consistent evidence for intermittency in the solar wind and transition region for both quasi-parallel and quasi-perpendicular shocks, with peak kurtosis in the shock foot. Finally, we use an adapted method of calculating correlation length to measure the local stirring scale of the turbulence, and find significant differences between upstream and downstream plasma. Addressing the time taken to reach well developed turbulence, Kolmogorov-like spectral power laws arise in the inertial range approximately 30s (or $1.6R_E$) downstream of the shock in the quasi-perpendicular case, while for the quasi-parallel shock the time is closer to 2 minutes ($6.2R_E$). However, the correlation length transitioned almost instantaneously across the shock for the quasi-perpendicular shock, but took $1-2$ minutes for the quasi-parallel shock.

2 Data Set

We explore the bow shock transition using in situ data obtained by the Magnetospheric Multiscale (MMS) mission (Burch et al., 2015). Magnetic field data are provided by the fluxgate magnetometer (FGM) (Russell et al., 2014) and search coil magnetometer (SCM) (Contel et al., 2014). FGM and SCM data are analysed as a merged data set (FSM) (Argall et al., 2018). Particle data are provided by the Fast Plasma Investigation's

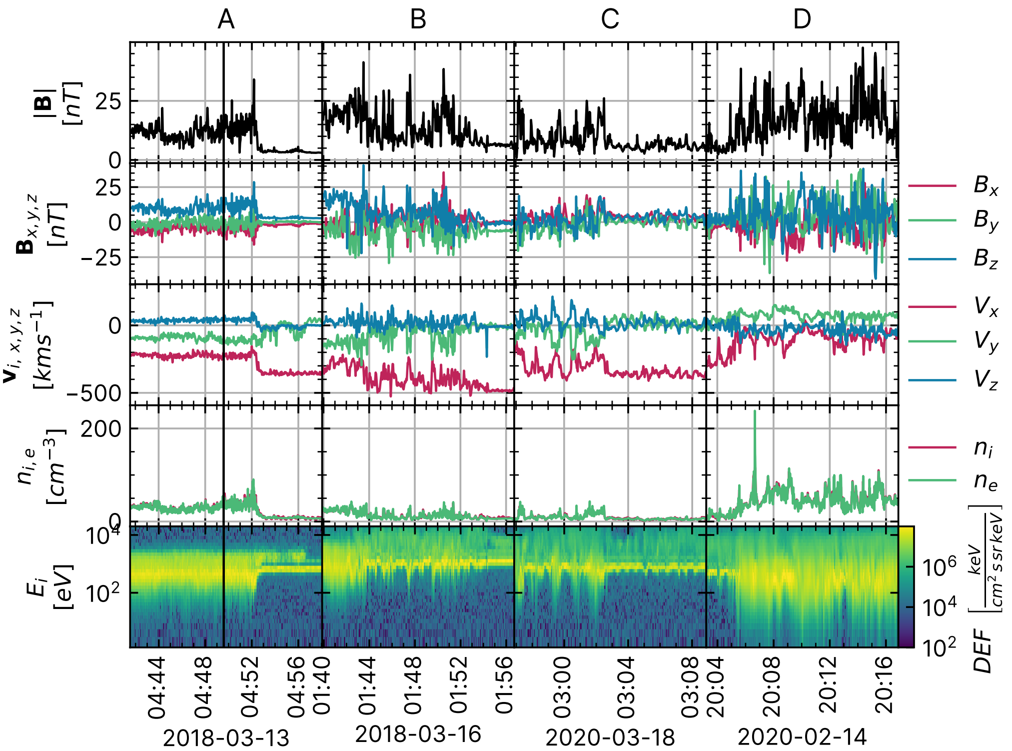

Figure 1. MMS observations showing events A (*left column*), and D (*right column*). *Row 1:* Magnetic field strength, $|\mathbf{B}|$; *Row 2:* Magnetic field components, $\boldsymbol{B}$, in GSE coordinates; *Row 3:* Ion velocity components, v_i (GSE); *Row 4:* Proton and electron densities, $n_{i,e}$; *Row 5:* Ion energy spectrogram. In events A-C, MMS travels from magnetosheath to solar wind, and in event D MMS travels from solar wind to magnetosheath. The shock normal angles are $\theta_{Bn} = 68^\circ, 41^\circ, 35^\circ, \& \, 33^\circ$ for A and D respectively. The timestamp of Figure 3 is indicated by a vertical black line in the left column.

(FPI) (Pollock et al., 2016) Dual Electron Spectrometer (DES) and Dual Ion Spectrometer (DIS). In high-resolution burst mode, the SCM and FSM magnetic fields are available at a sampling cadence of $f_s = 1/8192$ s, while FGM is available at 1/128 s. Particle moments are available at a cadence of 0.15 s and 0.03 s for ions and electrons, respectively.

Four high-resolution (burst) bow shock crossing intervals have been analysed here. The events were chosen to cover a range of bow shock angles from quasi-perpendicular to quasi-parallel, where the burst interval was longer than approximately 10 minutes. Event D was found with the help of a database of 2797 shocks compiled using machine learning, from Lalti et al. (2022). These four shocks were chosen firstly due to the intervals each recording sufficient burst data both upstream and downstream of the shock, allowing us to observe the evolution. Secondly, they all performed well on the test of Taylor's hypothesis, described further in section 2.1. Figure 1 provides a summary of events A and D, the most parallel and most perpendicular of the four events studied. The intervals on 13 March 2018, 16 March 2018, 18 March 2020 and 14 February 2020 are referred to as intervals A, B, C and D respectively. Note that electron moments are not available for MMS 4 during event D. All events are $\sim$ 15 minutes in duration. Table 1 shows plasma parameters averaged over the entire upstream interval, including electron upstream flow speed v_0, the acute angle between upstream magnetic field, $\mathbf{B}$, and the shock normal, θ_{Bn}, Alfvén Mach number M_A of the upstream flows, and the ion plasma beta β_i. The derived parameters M_A and β_i, along with observed values for v_0 and the magnetic field, were obtained from OMNI (King, 2005). The shock angle θ_{Bn} was calculated using a model from Peredo et al. (1995), using the upstream magnetic field lagged to the bow shock from OMNI and FPI moments from MMS. Sample standard errors on the angle were low for each of the events, with a maximum of $\pm 3.0°$ for event B.

The angle between the upstream magnetic field and shock normal angle, θ_{Bn}, decreases from quasi-perpendicular (68°) in event A to quasi-parallel (33°) in event D. Quasi-perpendicular shocks are characterised by near discontinuous transitions from the solar wind to bow shock. In contrast, a quasi-parallel shock has a more gradual transition and can often be complicated by upstream waves and instabilities caused by backstreaming ions in the foreshock. Therefore, the expectation is that structures created by the shock are more distinct in quasi-perpendicular shock crossings but are only observed for a short time, whereas a quasi-parallel shock will display complex behaviour that is more challenging to separate from the solar wind or magnetosheath.

Table 1. Average upstream plasma properties as observed by OMNI and MMS. Data from OMNI were averaged over the same duration as MMS.

Interval	$\theta_{Bn}[°]$	$v_0[kms^{-1}]$	M_A	β_i	Start yyyy/mm/dd hh:mm:ss	End
A	68 ± 0.6	356.4 ± 1.0	14.6 ± 1.1	4.4 ± 0.7	2018/03/13 04:41:33	04:58:02
B	41 ± 3.0	475.8 ± 4.7	9.0 ± 0.7	1.4 ± 0.3	2018/03/16 01:39:53	01:56:43
C	35 ± 1.1	394.4 ± 3.9	9.8 ± 0.8	2.2 ± 0.5	2020/03/18 02:56:53	03:08:52
D	33 ± 0.8	330 ± 2.4	14.6 ± 0.3	1.1 ± 0.9	2020/02/14 20:03:13	20:16:52

2.1 Validity of Taylor's Hypothesis

The interpretation of results in Section 3 relies on the validity of transforming the temporal domain measurements from MMS1 into the spatial domain, assuming the Taylor hypothesis. The assumption is that fluctuations will travel past the spacecraft at a bulk flow speed v_0 that is much greater than the wave propagation speeds, thus the spatial configuration of the fluctuations is unchanging as they are swept past the spacecraft. For plasmas with a fast flow speed, $v_0 \gg v_A$, such as the solar wind, this assumption is well founded. However, for plasmas such as the magnetosheath and the bow shock Taylor's hypothesis may not be valid.

The increments of the magnetic field, $\delta\boldsymbol{B}$, are given by:

$$\delta\boldsymbol{B}(\tau) = \langle|\boldsymbol{B}(t+\tau) - \boldsymbol{B}(t)|\rangle_T \tag{1}$$

where τ represents the time lag, and $\langle\rangle_T$ represents the mean over the full time interval. The lag τ can be transformed into spatial lag ℓ according to Taylor's hypothesis using the bulk flow speed: $\ell = v_0 t$. In this case, v_0 is the mean bulk velocity in each region (solar wind, bow shock or magnetosheath).

We can also measure the magnetic field increments for spatial lag ℓ directly using the separation between spacecraft pairs, without needing to assume Taylor's hypothesis. The equation in this case is then:

$$\delta\boldsymbol{B}(\ell_{ij}) = \left\langle|\boldsymbol{B}^i(t) - \boldsymbol{B}^j(t)|\right\rangle_T \tag{2}$$

where $i, j = 1, 2, 3, 4$ are labels for each of the four spacecraft, then ij indicates one of the six spacecraft pairs, and $\boldsymbol{B}^i$ indicates the magnetic field vector as measured by spacecraft i. We are therefore able to test the validity of Taylor's hypothesis by direct comparison of the amplitude of the magnetic field increments for single and multi-spacecraft measures. However, the nature of this test means that comparisons can only be made for scales close to the separation of the six MMS pairs. Therefore, good performance of this test at the spacecraft separation scales does not necessarily guarantee good performance at larger or smaller spatial scales.

We assess the validity of Taylor's hypothesis separately in each of the three regions (upstream, shock and downstream) for events A and D here, in Figure 2, with corresponding plots for events B and C shown in the supplementary material, Figure S1. Figure 2 shows magnetic fluctuation amplitude normalised to average field strength, $|\delta\boldsymbol{B}|/B_0$, for both single spacecraft and for the six spacecraft pairs (as in Chen & Boldyrev, 2017).

We found that all events performed reasonably well at the available spacecraft separation scales, particularly in the magnetosheath. The shock transition in event A sees the fluctuation amplitude slightly underestimated, indicating that the structure of the plasma is rapidly evolving in this region. In the solar wind in event A, it appears the plasma encountered by MMS 1 and 2 compared to MMS 3 and 4 was slightly different, leading to two different groups of single spacecraft lines. Chasapis et al. (2017) showed that there can be some variation in the second order structure function at the MMS separation scale when comparing single and multi spacecraft methods, even for intervals of pure solar wind. We will therefore not discount intervals where performance in the solar wind is not perfect. Event D performs best overall with single spacecraft measurements in all regions being very close to the multi spacecraft results.

3 The Magnetic Spectrum

In order to examine the evolution of the magnetic spectrum, events A-D were split into consecutive, non-overlapping windows containing 6 seconds of data per window.There are 145, 112, 79, and 133 windows for each event A-D, resulting in $N \approx 4 \times 10^4$ FSM field measurements per window, along with 40 ion measurements and 200 electron measurements. The power spectrum of $\boldsymbol{B}$ in the spacecraft frame is given as, $PSD(\boldsymbol{B}, k)$,

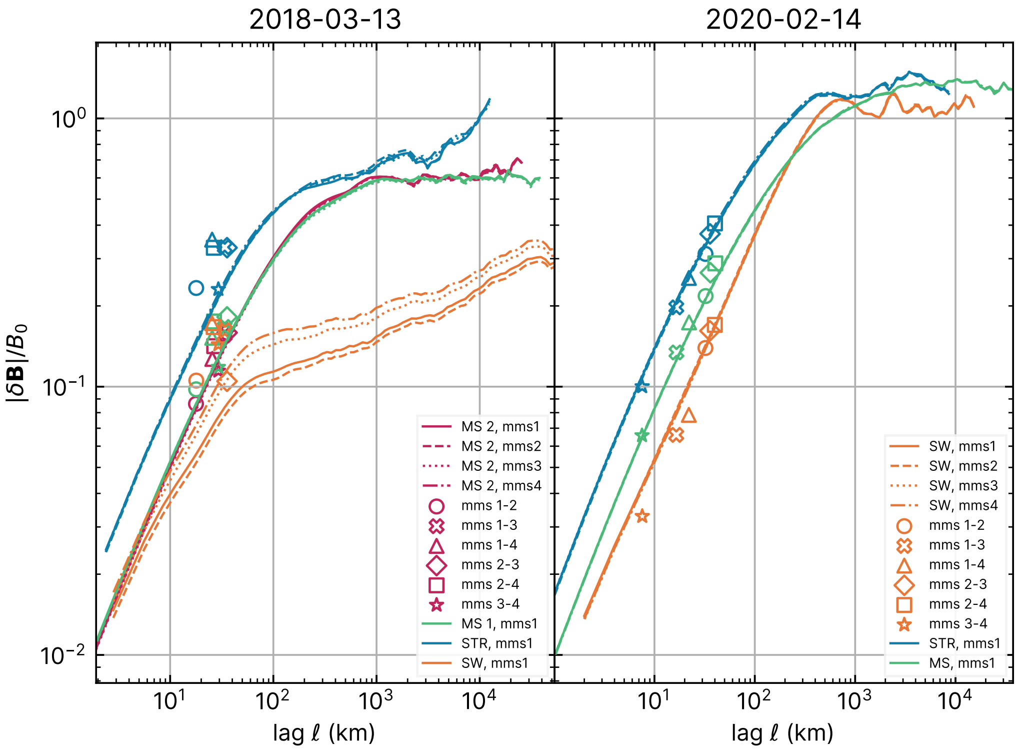

Figure 2. Magnetic fluctuation amplitude normalised to average field strength, $|\delta \boldsymbol{B}|/B_0$ as a function of scale ℓ. *Left:* Event A, *right:* event D. Fluctuation amplitude obtained using a single spacecraft and assuming Taylor's hypothesis is given by a line, solid for MMS 1, dashed for MMS 2, dotted for MMS 3, and dot-dashed for MMS 4. Colours represent the different regions of each event: Orange for solar wind (SW), blue for shock transition region (STR), and green/red for the magnetosheath (MS). Measurements from the six spacecraft pairs, with ℓ equivalent to the separation scale, are shown by the following markers: Circle for MMS 1-2, cross for 1-3, triangle for 1-4, diamond for 2-3, square for 2-4, and star for 3-4. In event A the single spacecraft and multi spacecraft results are reasonably similar, particularly in the magnetosheath. The results for event D are also extremely close at all scales and for all regions.

where $k = 2\pi f/v_0$, v_0 is the average flow speed in each region and f is a discrete frequency increment in the range $N/f_s \leq f \leq f_s/2$. The transformation of frequency f to wavenumber k is performed assuming Taylor's hypothesis, which is discussed in-depth in section 2.1. We calculate the trace power spectrum of the magnetic field, where components $B_{x,y,z}$ are pre-filtered with a Hanning window, and we take the sum of the power in the three components i.e. $P = \sum_i P(B_i)$..

In turbulent plasmas, the magnetic spectrum often appears as a series of power laws with varying indices, $P \propto k^\alpha$ (Frisch, 1995). For example, power-law index $\alpha = -5/3$ corresponds to the inertial range of fluid turbulence (Kolmogorov, 1941), typical of space plasmas at spatial scales far above ion kinetic scales. At the ion scales, $\sim d_i$ or $\sim \rho_i$, solar wind and magnetosheath plasmas typically exhibit a breakpoint below which the magnetic spectrum steepens. In this ion kinetic range, the power-law index α is variable, though $\alpha \approx -2.8$ is typical for the solar wind (Alexandrova et al., 2009; Sahraoui et al., 2010). The breakpoint between the fluid MHD scale and the ion kinetic scale has been seen at the larger of d_i, or ρ_i (Chen et al., 2014) when observing solar wind undisturbed by the bow shock. A second breakpoint is often observed at electron kinetic scales, and again the slope of the magnetic spectrum is expected to steepen in the electron kinetic range, below $\sim d_e$. Hence, the magnetic spectrum is expected to comprise three or more distinct power laws with different slopes. In order to characterise the power laws of our observed magnetic spectra, we seek an algorithm that can generate and fit an arbitrary number of straight lines to a spectrum, with a variable number of breakpoints. Hence, we use the Multivariate Adaptive Regression Splines (MARS) algorithm, developed by (Friedman, 1991), and implemented by (Milborrow et al., 2011). Additionally, the MMS noise floor was found to be reached at wavenumbers of approximately $k \approx 10km^{-1}$, therefore the spectra at $k \geq 10km^{-1}$ has been excluded from the MARS fit. This was found to significantly reduce the effect of the noise floor, although it does appear in some windows as spectral indices ≥ 0 at the largest k.

Figure 3 shows an example of a spectrum obtained when MMS was downstream of the shock during event A, with the resultant MARS fit overlaid. Examples from the solar wind and magnetosheath, and for event D can be found in the supplementary material as Figure S2. We also note that an electron scale wave is visible at $k \approx 2\,\mathrm{km}^{-1}$ as a peak in the spectrum. Similar structures appear in other intervals and are characterised by a dramatic change from positive to negative power law index at the electron scale. This demonstrates that the MARS method is able to identify spectral features associated with wave activity, and allow interpretation of them separately from the background turbulent spectrum.

Figures 4 and 5 show the evolution of spectral index with time for the intervals A and D, respectively. Equivalent plots are given for events B and C in the supplemental material, Figures S3 and S4. Each 6 second window is represented as a vertical slice where the spectral index at a given scale is represented by the colour of the vertical bar. The extent in k over which that scale applies is given by the height of the bar, with each slice in time usually having 3 or more distinct slopes covering the observed spectrum.

In Figure 4, we see that in the solar wind immediately preceding the shock, the breakpoint between the inertial (MHD) range and the ion (kinetic) range is much less than both d_i and ρ_i. As in Figure 3 above, this observation differs from studies, e.g. Chen et al. (2014), who suggest that in undisturbed solar wind, the spectral break should be d_i or greater. However, in the magnetosheath close to the shock, we find that the breakpoint shifts to larger scales and settles in the expected range $d_i \leq BP \leq \rho_i$. This is most likely due to the lack of clean, undisturbed solar wind very close to the bow shock.

For event D, Figure 5, the spectral slope in the solar wind is much steeper than expected at spatial scales larger than the ion inertial length, with $\alpha \sim -4$ on average. This feature may be caused by an upstream wave for which the peak wavelength is greater

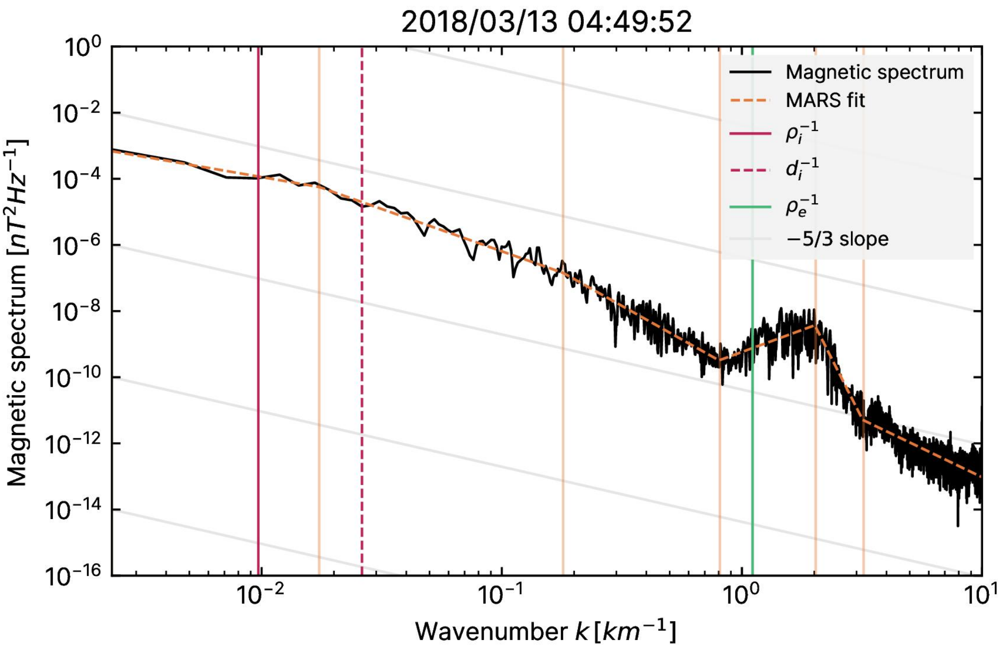

Figure 3. A plot of magnetic spectrum for an example ~ 6 s window downstream of the shock on 13/03/2018, illustrated as a vertical black line on Figure 1. Grid lines are shown with a slope of $-5/3$. The magnetic spectrum is shown in black. The ion and electron scales ($\rho_{i,e}$ and d_i) are shown as red and green vertical lines. The fit to the spectrum is shown as an orange dashed line, built from chained linear regressions using the MARS method. Vertical orange lines highlight breakpoints determined by the MARS fit. An electron scale wave is visible at approximately $k \approx 2/\rho_e$, and this is reflected in the MARS fit by steep upward and downward slopes. The part of the spectrum which exceeds the noise floor at $k \approx 10km^{-1}$ has been excluded from this plot.

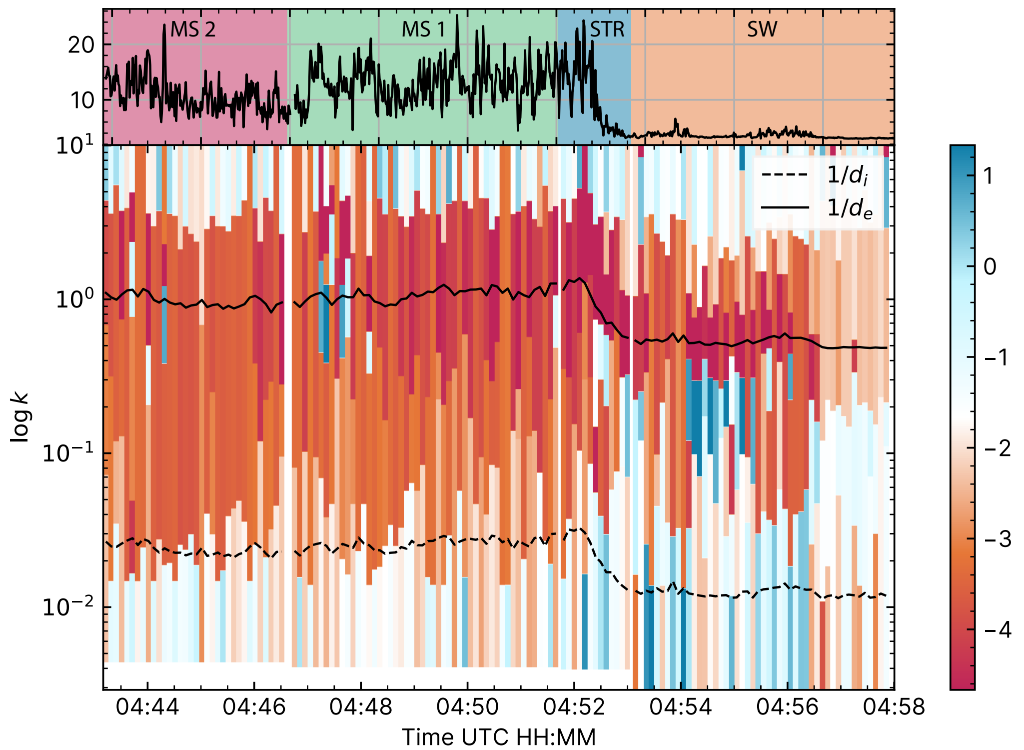

Figure 4. Evolution of spectral slopes as a function of time for event A. *Top:* Magnetic field strength, $|\boldsymbol{B}|$. Colours refer to magnetosheath (MS 1/2), shock transition region (STR) and solar wind (SW) *Bottom:* Evolution of spectral indices from MARS fit. Note that this does not always split the spectrum into three regions. The colour represents the slope of the power-law fit. Red indicates steeper than $-5/3$, while blue is shallower than $-5/3$. Breakpoints are indicated by a change in colour. Electron scales, $\rho_e \approx d_e$ are shown as a solid black line, and ion scales d_i and ρ_i are dashed and dot-dashed black lines. Event A is a quasi-perpendicular shock and as a result we get a clear distinction between solar wind and magnetosheath spectra. The ion-inertial breakpoint (BP) is $k \gg 1/d_i$ in the solar wind and rapidly transitions to $1/d_i > k > 1/\rho_i$ in the magnetosheath.

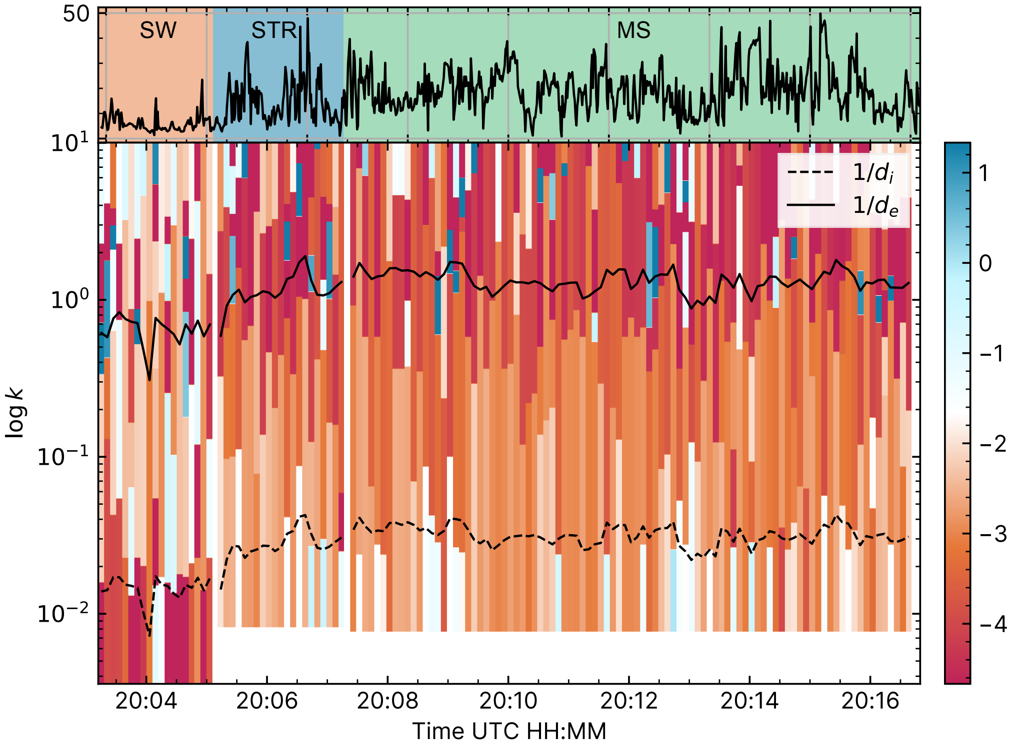

Figure 5. Equivalent to Figure 4 for interval D, 20/03/2020. There are many windows where the breakpoint is aligned with $1/d_i$ throughout the whole event. In the magnetosheath the breakpoints move from shallower to steeper with increasing k, but in the solar wind the opposite is true and the spectrum is steeper when $k < 1/d_i$.

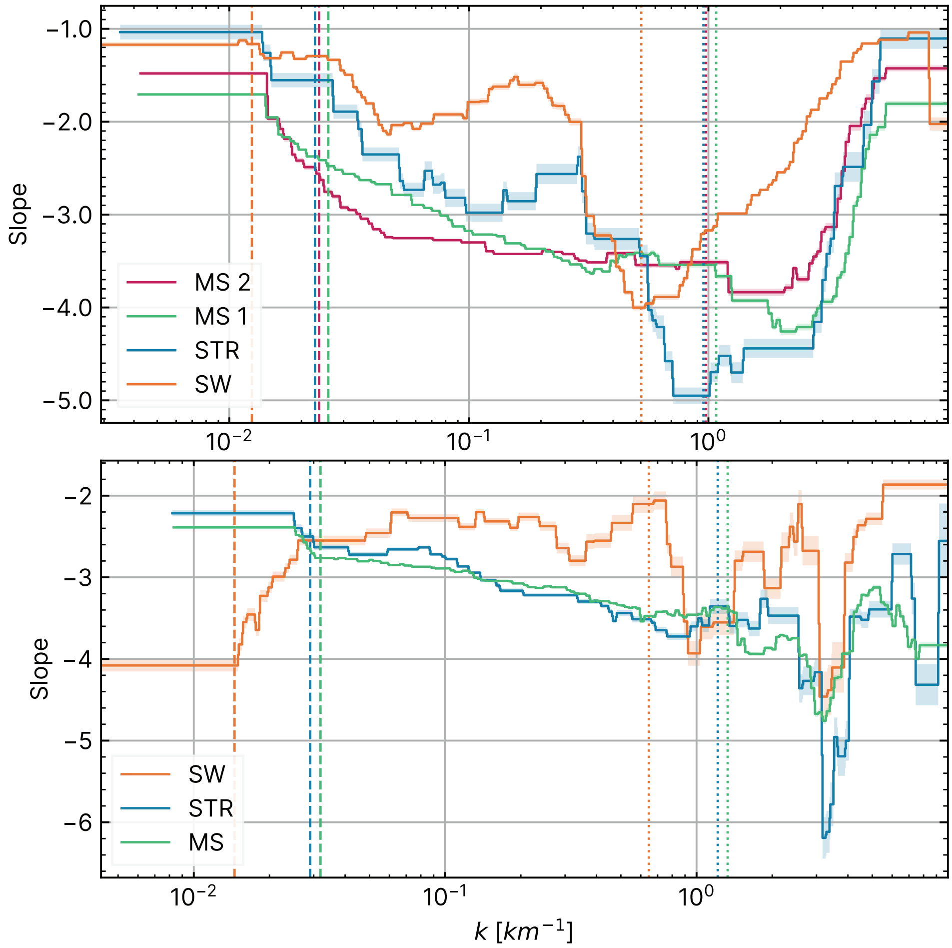

Figure 6. Average slope as a function of scale for event A (quasi-perpendicular), *top*, and event D (quasi-parallel), *bottom*. Each line represents a subsection of the entire interval, i.e. magnetosheath (MS - red or green), the shock transition region (STR - blue), or solar wind (SW - orange). The 'MS 2' line is further downstream than 'MS 1'. See Figures 4 and 5 for a definition of the boundaries. Average kinetic scales, d_i and d_e, are also plotted as dashed and dotted vertical lines, respectively. We see that there are occasions in both panels where the STR spectral index lies outside of the transition between SW and MS.

than the maximum resolvable within each $6s$ window. This steep spectral slope is not observed in the shock transition or magnetosheath. Downstream of the shock, the breakpoint between inertial and ion scales tracks well with d_i for most windows. In the inertial range, we observe a steady spectral slope of $\alpha \sim -5/3$ approximately 1 minute after the spacecraft crosses the shock ramp.

Figure 6 shows the average slope as a function of scale, k, for intervals A and D, broken down into subsections based on MMS's location in relation to the shock, e.g. magnetosheath (MS), in the shock transition region (STR), or the solar wind (SW). The chosen intervals corresponding to each region are shown in the top panels of Figures 4 and 5.. Similar figures for intervals B and C are given in the supplemental material, Figures S5 and S6. Errors shown are sample standard deviations from all windows within the region. For a 'quiet' boundary layer that introduces no new fluctuations to the medium, and instead is simply a superposition of modes either side, we might expect the spectral slope within that boundary to be between the slope either side. For such a shock, the slope in the STR would be between those in the SW and MS at all scales. That is, we would see the blue line (slope in the STR) between the green (MS) and yellow (SW) lines at all scales, as this would indicate that it is purely a transitional state as solar wind plasma crosses the shock and into the magnetosheath. However, we expect the shock to introduce new waves and instabilities. This is apparent for the given events where the STR slope is outside of the MS and SW lines. In event A, we see this most prominently at electron scales ($k \approx d_e$), whereas for event D, this occurs at $k \approx 3d_e$. We also note the extremely steep slope in the inertial range for the solar wind in event D, which was also visible in Figure 5. However, for most scales the shock transition region lies between the SW and MS lines, or very close to the MS. The source of the steeper shock transition region at electron scales could be due to similar scale instabilities or other non-turbulent fluctuations at the shock, or an indication of a more efficient turbulent energy dissipation process.

Comparing the average slopes in Figure 6 to recent statistics from Li et al. (2020) of the magnetosheath close to the bow shock at MHD and sub-ion scales, we find that event A compares well in both regions, and event D agrees with statistics in the sub-ion range. In event A the slope in the MHD range is ~ -1.7, compared to -1.47 ± 0.24 found by Li et al. (2020) for quasi-perpendicular shocks. In the sub ion range the slope is ~ -3.3 at the midpoint between ρ_i and ρ_e, compared to -2.97 ± 0.65. For event D the MHD slope is ~ -2.2 compared to -1.46 ± 0.38, while for sub-ion scales the slope is ~ -3.1 at the midpoint, compared to -2.84 ± 0.15 from Li et al. (2020). This shows that Event A is a more 'typical' quasi-perpendicular shock while event D has steeper slopes at both MHD and sub ion scales than might be expected for a typical quasi parallel shock.

4 Kurtosis

A fundamental method for studying intermittency is to examine deviations from Gaussianity in the distribution of magnetic field fluctuations, for which a typical method is to use the kurtosis (Matthaeus et al., 2015). Intermittency is defined as strong, highly localised gradients, especially at small scales. If the kurtosis $\kappa(\boldsymbol{B}) > 3$, then the magnetic field has an overabundance of extreme gradients relative to a normal distribution, which therefore indicates the existence of intermittent structures. $\kappa \leq 3$ indicates that intermittency is not present.

Figure 7 shows the kurtosis, independent of scale, for events A and D. Events B and C are shown in the supplemental material as Figures S7 and S8. The kurtosis is calculated for consecutive windows containing 10^5 samples, based on the rule of thumb $p_{max} = \log N - 1$, where p_{max} is the maximum moment (i.e. fourth) and N is the number of samples (Dudok de Wit et al., 2013). In event A, we see a clear difference in kurtosis between the solar wind and magnetosheath. Intermittency is present upstream of the shock, but there are very few occasions where $\kappa > 3$ in the downstream. The kurtosis peaks to over 20 a few seconds after the spacecraft crosses the shock ramp into the solar wind in event A. In event D, we see the kurtosis peaking in the solar wind before the shock transition region, but the peak is much lower at ~ 6, about one quarter of the peak in event A. Following the shock there is a period of Gaussian kurtosis ($\kappa \sim 3$), and even some times where the distribution is platykurtic ($\kappa < 3$). However, the kurtosis does begin to increase again further into the magnetosheath. This could be due to motion of the shock front towards the spacecraft, causing a partial crossing.

In order to directly compare the prevalence of intermittent fluctuations across the shock, we next examine the difference between the proportion of bins with $\kappa > 3$. For

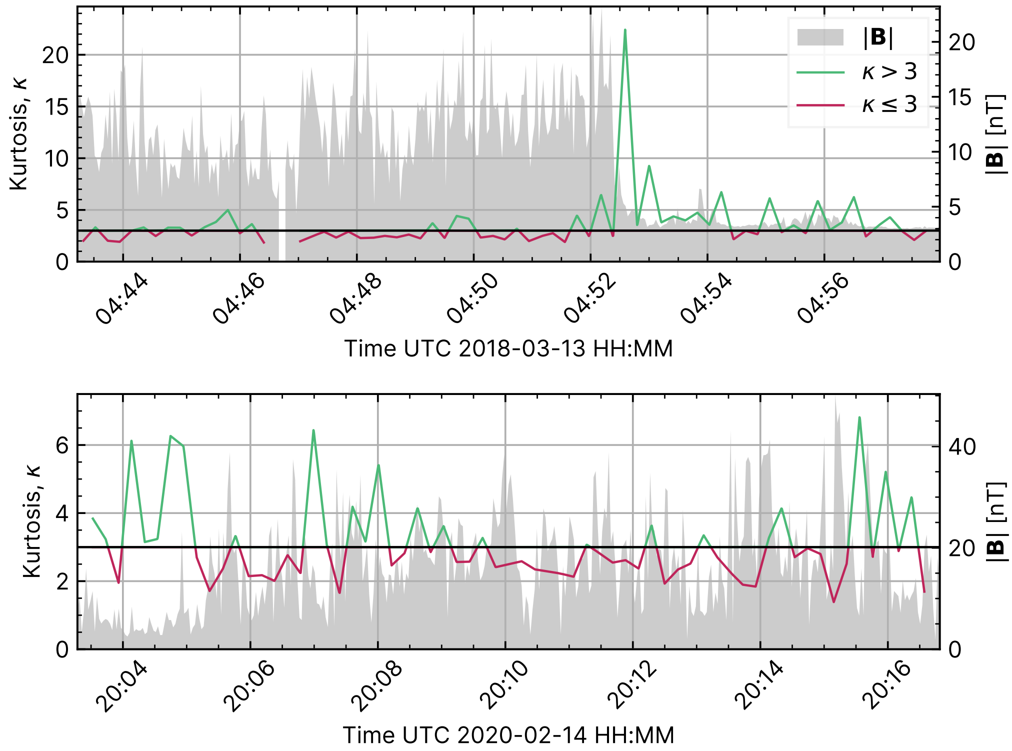

Figure 7. Kurtosis examined for events A (*top*) and D (*bottom*). $\kappa > 3$ is shown green, and $\kappa \leq 3$ is red. A horizontal black line highlights $\kappa = 3$. $|\boldsymbol{B}|$ is displayed for reference as a grey shaded background, with the vertical scale on the right. The quasi-perpendicular event A shows a clear difference between solar wind and magnetosheath, with κ peaking in the shock foot. The quasi-parallel example (event D) shows a similar relationship, however towards the end of the interval κ begins increasing again.

event A, we find that there is a large change across the shock: In the solar wind 60.7% of bins show signs of intermittency, whereas 31.8% of bins do in the magnetosheath. For quasi parallel event D we observe a lower proportion of intermittent intervals in the upstream, with 50.0% in the solar wind, and a similar proportion to event A, 31.4%, in the magnetosheath.

Therefore, in comparing the kurtosis observed in quasi-parallel and quasi-perpendicular shocks, we find that there are significant changes between the upstream and downstream distributions. The solar wind close to the shock and the shock foot have significantly higher kurtosis than the magnetosheath. This is visible in both the quasi-parallel and quasi-perpendicular case. However, the peak kurtosis is significantly higher for the quasi-perpendicular event by a factor of approximately 4.

5 Correlation Length

Next, we seek to measure the characteristic size of turbulent fluctuations in the magnetic field. Energy is typically transferred in a 'cascade' from large to small scales on average, generating magnetic structures at sizes ranging from stirring scales to the scales at which energy is dissipated. The correlation length, λ_c, quantifies the average size of the largest scale fluctuations visible in the data (Stawarz et al., 2019, 2022) which can be associated with the 'stirring' scale, providing the dataset covers a portion of space significant enough for large correlation lengths to be observed. Using the autocorrelation function of magnetic fluctuations, given by:

$$R(l) \equiv \frac{\langle \mathrm{Tr}[\delta \boldsymbol{b}(\boldsymbol{x}+l)\delta \boldsymbol{b}(\boldsymbol{x})] \rangle}{\langle |\delta \boldsymbol{b}|^2 \rangle}, \tag{3}$$

We define the correlation length as follows:

$$\lambda_c \equiv \int_0^\infty R(l)\, dl. \tag{4}$$

Where Tr[...] is the trace, $\delta \boldsymbol{b} \equiv \boldsymbol{B} - \langle \boldsymbol{B} \rangle$ and l is the lag of the autocorrelation. This calculation is achieved by integration up to the first zero crossing of $R(l)$, or by a fit of the form $R(l) \propto \exp(-l/\lambda_c)$. We find that results do not differ significantly between methods, and we therefore present results using the integration method.

Correlation length generally relies on having a data set long enough for a correlation function to become uncorrelated. However, the region of space near the bow shock is a rapidly changing environment dominated by processes unrelated to turbulence. Care is therefore needed when selecting what scale of fluctuations should be included. Any window of time that includes the shock will have a correlation length that is closely related to the crossing time of the shock.

In this case, it is more descriptive to examine fluctuations at scales smaller than the step-function introduced to the time series by the shock. Therefore, we use a variable high-pass filter over the event to remove the effect of low frequency variations, such as the shock ramp. A 10^{th} order Butterworth filter was used, which can be defined by the critical frequency, $F_{crit} \equiv 1/T_{max}$ where T_{max} is the longest time allowed by the filter. By varying T_{max}, the data is limited exclusively to fluctuations with wavelength shorter than $v_0/2F_{crit}$. If T_{max} is less than the period associated with the stirring scale of the turbulence, then the measured λ_c will have a dependence on the size of the filter, increasing in proportion to T_{max}. When T_{max} becomes greater than the period associated with the stirring scale, λ_c will appear to plateau, and changes in T_{max} will not have a significant effect on λ_c. Filtering λ_c in this manner provides information on coherence scales at, crucially, scales $\leq T_{max}$. I.e. With this method we do not capture coherence at large scales, most notably in the solar wind. However in the bow shock and magnetosheath, as well as in foreshock structures, we find that this method works well.

Similar to the approach used when discussing the magnetic spectrum, we have split the interval into smaller consecutive windows. The range of T_{max} was chosen to cover several decades in duration, and are approximately logarithmically spaced. The entire event is filtered according to T_{max} before being split into windows. Figure 8 describes the evolution of the frequency-dependent correlation length for event A. Plateaus - areas without a significant change in colour between adjacent T_{max} bins - indicate that a consistent correlation length has been reached. We see that in the solar wind, a consistent λ_c is not reached; the maximum observed correlation length is over $100d_i$. However, if burst data was available further into the solar wind we would likely have seen this increase far higher, given that solar wind correlation lengths have been measured by the ACE spacecraft at the L1 Lagrange point to be $0.03 - 0.08AU$, which is approximately $50 - 100 \times 10^3 d_i$ (Ragot, 2022). In the magnetosheath we see a very clear plateau of $3 - 10d_i$ immediately downstream of the shock, which appears to slowly increase further into the magnetosheath. At the point in the magnetosheath furthest from the shock $(04:42)$, the correlation length may still be in a plateau but with $\lambda_c > 10d_i$.

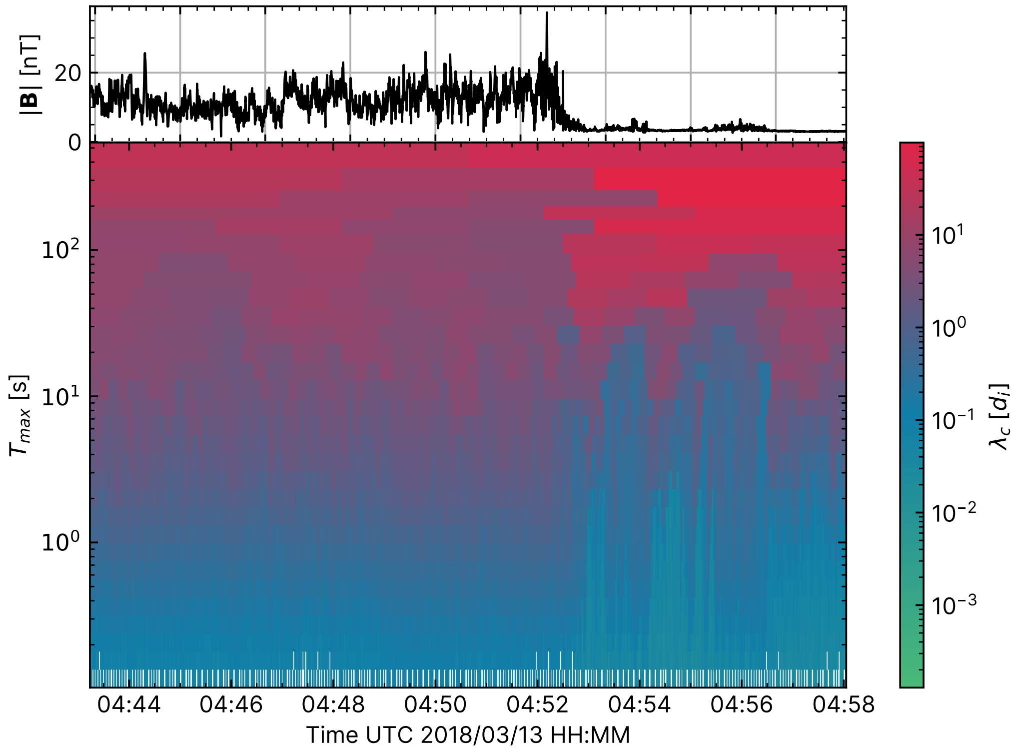

Figure 8. *Upper*: Magnetic field strength, $|B|$. *Lower*: Correlation length, λ_c, colour (units of ion inertial length), as a function of time and T_{max}. The width of each bin is equal to T_{max} up to T_{max} = total interval length/2. A plateau, which can be seen in areas where the colour (λ_c) does not change significantly when moving up to a larger T_{max}, indicates that the fluctuations are correlated on scales equal-to or smaller-than T_{max}. There is an observable difference in λ_c before and after the shock; a large plateau exists between $\lambda_c = 3$ and $\lambda_c = 10$ immediately downstream of the shock, but in the region upstream of the shock transition region λ_c exceeds $100d_i$.

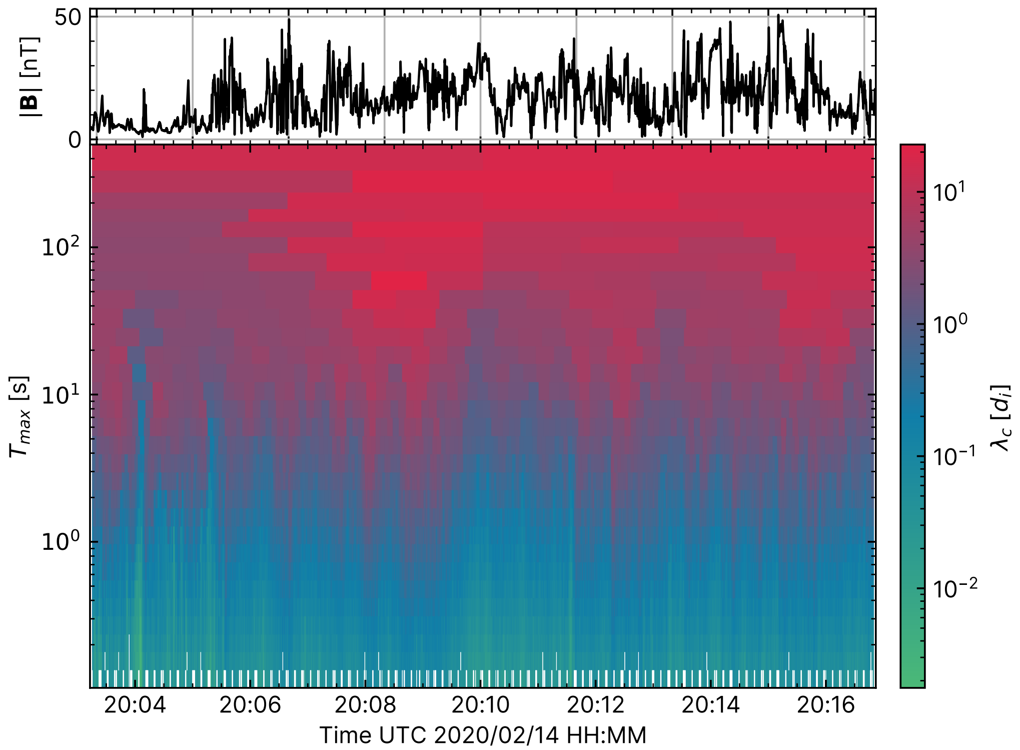

Figure 9. Similar to Figure 8 for event D. In this event, correlation length appears to increase on the magnetosheath side.

Figure 9 shows an equivalent plot for the quasi-parallel event, D. The correlation length on the SW side is approximately $\lambda_c = 3 - 10d_i$. There is a foreshock structure at 20:04 UTC which may be a partial shock crossing. This indicates that this may not be representative of the solar wind, and is instead an extended shock transition region or foreshock. These structures may reduce the average correlation length, similar to Figure 8. The correlation length after the shock also appears to be in the range $\lambda_c = 10{-}12d_i$, approximately the same as what is observed for the quasi-perpendicular event A. These correlation lengths can be compared to recent results from Stawarz et al. (2022), who found that $\lambda_c \approx 10s$ of d_i at the sub solar magnetosheath, gradually increasing to $100s$ of d_i in the flanks. For the shocks analysed here, MMS entered the sheath in or close to the sub solar region, therefore our results are consistent.

Finally, there are indications that shock micro-structure and non-stationarity may also have an effect on the correlation length. In the quasi-perpendicular case, Figure 8, we see two periods of upstream wave activity visible at 04:54 and 04:56 in the top panel, both approximately sixty seconds in duration. This causes a significant reduction of λ_c of approximately a factor of 10 compared to the immediate surroundings, but only for $T_{max} \leq 60s$. Similar structure is also visible to a lesser extent within the shock ramp at 04:52:30. These upstream wave packets may be partial crossings of the shock foot caused by ripples on the shock surface (Johlander et al., 2016). Hence, the features in the filtered correlation length may be associated with fluctuations in the foot and ramp arising from this form of non-stationarity. They also appear at larger scales (longer T_{max}) further from the shock, and smaller scales (shorter T_{max}) closer to the shock, which is perhaps evidence of structures transitioning from larger to smaller scales as the solar wind plasma approaches the shock. A similar effect is visible in Figure 9, where periods of large magnetic field amplitude are associated with lower correlation length than the surroundings. However, they are shorter in duration, and we do not observe a reduction in correlation length closer to the shock. The occurrence of these structures would suggest the presence of narrow band waves generated in the shock transition region.

6 Conclusions

In this study, we used three different measures of turbulence, the magnetic spectrum, scale-independent kurtosis and correlation length, to explore the evolution of the solar wind and magnetosheath turbulence across Earth's bow shock. The influence of the bow shock transition region on the properties of turbulence is not currently well understood. Therefore, by using the magnetic spectrum to observe differences in the turbulent energy cascade, the kurtosis to explore the properties of intermittency and the correlation length to describe changes in coherence scales, we aim to produce a representative picture of how turbulence evolves from the solar wind, across the bow shock, and downstream into the magnetosheath. We therefore address the following questions: 1) Is there a measurable difference between turbulence seen in the bow shock transition region and in the surrounding plasma? And 2) How quickly does well developed turbulence arise in the magnetosheath after a bow shock crossing?

We find that the shock transition region displays features in the spacecraft frame magnetic spectrum that are different to the turbulence present in the solar wind and magnetosheath. This can be seen as shock transition spectral slopes which are steeper at scales where $k \geq d_e$ than either of their upstream or downstream neighbours (Figure 6). This suggests shock processes are driving scale dependent energy dissipation at sub-electron scales. This is observed at both quasi-parallel and quasi-perpendicular shocks (events A and D, $\theta_{Bn} = 68°$ and $33°$ respectively). However, we note that these signatures are not always so clearly observable, which is the case for events B and C. Figures showing structure (or lack thereof) in the magnetic spectral indices and scale-independent kurtosis are shown for events B and C in the supplemental material. We find that the breakpoint (BP) separating the inertial range from the ion range transitions from $BP << d_i$ before the shock, to $d_i \leq BP \leq \rho_i$ in the magnetosheath.

Finally, we have adapted the definition of correlation length to include a high-pass filter defined by a critical frequency F_{crit}, which allowed us to calculate a turbulent correlation length across the shock that effectively removes the large-scale spectral influence of the shock. We found that close to the shock the correlation length is longer on the solar wind side than the magnetosheath side. Plateaus in high-pass filtered correlation length averaged $25d_i$ in the solar wind and $< 20d_i$ in the magnetosheath. This relates to a reduction in size of the stirring scale in the magnetosheath when compared to solar wind close to the shock. We found that upstream structures in the shock transition region introduce plateaus of reduced correlation length for short periods of time, on the order of 10s of seconds.

The magnetic spectrum transitioned from solar wind-like to magnetosheath-like over a $20s$ interval for event A and a 1 minute interval for event D. This corresponds to $180d_i$ and $1.1R_E$ for event A, and $600d_i$ and $3.1R_E$ for event D. Additionally, the intermittency (kurtosis $\kappa > 3$) seen in the upstream transitioned to the average magnetosheath (non-intermittent) level after 30s ($267d_i$ or $1.7R_E$) in the quasi-perpendicular case, whereas for the quasi-parallel shock, intermittency was still present until two minutes ($1.2 \times 10^3 d_i$ or $6.2R_E$) after the shock crossing. With regards to the correlation length, the quasi-perpendicular case demonstrated a rapid ($\sim 6s$) transition from solar wind-like scales to magnetosheath-like scales on crossing the shock ramp. In the quasi-parallel case, however, the transition was much slower, occurring over a period of approximately 2 minutes. Together these results suggest that the time needed for the turbulent fluctuations to fully develop after crossing the shock ramp is dependent on θ_{Bn}

We note that the case studies shown here may not be representative of all shocks. The natural next step is therefore to to determine whether the conclusions reached here are representative of the typical quasi-parallel or quasi-perpendicular shock. In a future work, we will compile a statistical survey of shocks across a range of shock normal angles and other plasma parameters, to explore the average behaviour of the bow shock. Additionally, we will explore the applicability of these methods to simulations.

Acknowledgments

J. Plank was supported by STFC studentship ST/V507064/1 (2502298). I. L. Gingell was supported by the Royal Society University Research Fellowship No. URF\R1\191547.

The data that support the findings of this study are openly available at the MMS Science Data Center at the Laboratory for Atmospheric and Space Physics (LASP) hosted by the University of Colorado, Boulder (`https://lasp.colorado.edu/mms/sdc/public/`), references (Burch et al., 2015; Ergun et al., 2014; Lindqvist et al., 2014; Torbert et al., 2014; Pollock et al., 2016), and NASA/GSFC's Space Physics Data Facility's OMNIWeb service (`https://omniweb.gsfc.nasa.gov/`, references (Lepping et al., 1995; Ogilvie et al., 1995; Smith et al., 1998; McComas et al., 1998).

References

Alexandrova, O. (2008, February). Solar wind vs magnetosheath turbulence and alfvén vortices. *Nonlinear Processes in Geophysics*, *15*(1), 95–108. Retrieved from `https://doi.org/10.5194/npg-15-95-2008` doi: 10.5194/npg-15-95-2008

Alexandrova, O., Chen, C. H. K., Sorriso-Valvo, L., Horbury, T. S., & Bale, S. D. (2013, August). Solar wind turbulence and the role of ion instabilities. *Space Science Reviews*, *178*(2-4), 101–139. Retrieved from `https://doi.org/10.1007/s11214-013-0004-8` doi: 10.1007/s11214-013-0004-8

Alexandrova, O., Saur, J., Lacombe, C., Mangeney, A., Mitchell, J., Schwartz, S. J., & Robert, P. (2009, October). Universality of solar-wind turbulent spectrum from MHD to electron scales. *Physical Review Letters*, *103*(16). Retrieved from `https://doi.org/10.1103/physrevlett.103.165003` doi: 10.1103/physrevlett.103.165003

Argall, M. R., Fischer, D., Le Contel, O., Mirioni, L., Torbert, R. B., Dors, I., ... Russell, C. T. (2018). *The fluxgate-searchcoil merged (fsm) magnetic field data product for mms.*

Bessho, N., Chen, L.-J., Stawarz, J. E., Wang, S., Hesse, M., Wilson, L. B., & Ng, J. (2022, April). Strong reconnection electric fields in shock-driven turbulence. *Physics of Plasmas*, *29*(4), 042304. Retrieved from `https://doi.org/10.1063/5.0077529` doi: 10.1063/5.0077529

Bessho, N., Chen, L.-J., Wang, S., Hesse, M., Wilson, L. B., & Ng, J. (2020, September). Magnetic reconnection and kinetic waves generated in the earth's quasi-parallel bow shock. *Physics of Plasmas*, *27*(9), 092901. Retrieved from `https://doi.org/10.1063/5.0012443` doi: 10.1063/5.0012443

Bruno, R., & Carbone, V. (2013). The solar wind as a turbulence laboratory. *Living Reviews in Solar Physics*, *10*. Retrieved from `https://doi.org/10.12942/lrsp-2013-2` doi: 10.12942/lrsp-2013-2

Burch, J. L., Moore, T. E., Torbert, R. B., & Giles, B. L. (2015, May). Magnetospheric multiscale overview and science objectives. *Space Science Reviews*, *199*(1-4), 5–21. doi: 10.1007/s11214-015-0164-9

Burch, J. L., Torbert, R. B., Phan, T. D., Chen, L.-J., Moore, T. E., Ergun, R. E., ... Chandler, M. (2016, June). Electron-scale measurements of magnetic reconnection in space. *Science*, *352*(6290). Retrieved from `https://doi.org/10.1126/science.aaf2939` doi: 10.1126/science.aaf2939

Carbone, V., Veltri, P., & Mangeney, A. (1990, August). Coherent structure formation and magnetic field line reconnection in magnetohydrodynamic turbulence. *Physics of Fluids A: Fluid Dynamics*, *2*(8), 1487–1496. Retrieved from https://doi.org/10.1063/1.857598 doi: 10.1063/1.857598

Chasapis, A., Matthaeus, W. H., Parashar, T. N., Fuselier, S. A., Maruca, B. A., Phan, T. D., … Strangeway, R. J. (2017, July). High-resolution statistics of solar wind turbulence at kinetic scales using the magnetospheric multiscale mission. *The Astrophysical Journal*, *844*(1), L9. Retrieved from https://doi.org/10.3847/2041-8213/aa7ddd doi: 10.3847/2041-8213/aa7ddd

Chasapis, A., Matthaeus, W. H., Parashar, T. N., Wan, M., Haggerty, C. C., Pollock, C. J., … Burch, J. L. (2018, March). In situ observation of intermittent dissipation at kinetic scales in the earth's magnetosheath. *The Astrophysical Journal*, *856*(1), L19. Retrieved from https://doi.org/10.3847/2041-8213/aaadf8 doi: 10.3847/2041-8213/aaadf8

Chen, C. H. K., & Boldyrev, S. (2017, June). Nature of kinetic scale turbulence in the earth's magnetosheath. *The Astrophysical Journal*, *842*(2), 122. Retrieved from https://doi.org/10.3847/1538-4357/aa74e0 doi: 10.3847/1538-4357/aa74e0

Chen, C. H. K., Leung, L., Boldyrev, S., Maruca, B. A., & Bale, S. D. (2014, November). Ion-scale spectral break of solar wind turbulence at high and low beta. *Geophysical Research Letters*, *41*(22), 8081–8088. Retrieved from https://doi.org/10.1002/2014gl062009 doi: 10.1002/2014gl062009

Contel, O. L., Leroy, P., Roux, A., Coillot, C., Alison, D., Bouabdellah, A., … de la Porte, B. (2014, September). The search-coil magnetometer for MMS. *Space Science Reviews*, *199*(1-4), 257–282. Retrieved from https://doi.org/10.1007/s11214-014-0096-9 doi: 10.1007/s11214-014-0096-9

Cranmer, S. R., Asgari-Targhi, M., Paz Miralles, M., Raymond, J. C., Strachan, L., Tian, H., & Woolsey, L. N. (2015, May). The role of turbulence in coronal heating and solar wind expansion. *Philosophical Transactions of the Royal Society A: Mathematical, Physical and Engineering Sciences*, *373*(2041), 20140148. Retrieved from https://doi.org/10.1098/rsta.2014.0148 doi: 10.1098/rsta.2014.0148

Dudok de Wit, T., Alexandrova, O., Furno, I., Sorriso-Valvo, L., & Zimbardo, G. (2013, May). Methods for characterising microphysical processes in plasmas. *Space Science Reviews*, *178*(2-4), 665–693. Retrieved from https://doi.org/10.1007/s11214-013-9974-9 doi: 10.1007/s11214-013-9974-9

Ergun, R. E., Tucker, S., Westfall, J., Goodrich, K. A., Malaspina, D. M., Summers, D., … Cully, C. M. (2014, December). The axial double probe and fields signal processing for the MMS mission. *Space Science Reviews*, *199*(1-4), 167–188. Retrieved from https://doi.org/10.1007/s11214-014-0115-x doi: 10.1007/s11214-014-0115-x

Franci, L., Cerri, S. S., Califano, F., Landi, S., Papini, E., Verdini, A., … Hellinger, P. (2017, November). Magnetic reconnection as a driver for a sub-ion-scale cascade in plasma turbulence. *The Astrophysical Journal*, *850*(1), L16. Retrieved from https://doi.org/10.3847/2041-8213/aa93fb doi: 10.3847/2041-8213/aa93fb

Franci, L., Landi, S., Matteini, L., Verdini, A., & Hellinger, P. (2015, October). HIGH-RESOLUTION HYBRID SIMULATIONS OF KINETIC PLASMA TURBULENCE AT PROTON SCALES. *The Astrophysical Journal*, *812*(1), 21. Retrieved from https://doi.org/10.1088/0004-637x/812/1/21 doi: 10.1088/0004-637x/812/1/21

Friedman, J. H. (1991, March). Multivariate adaptive regression splines. *The Annals of Statistics*, *19*(1). Retrieved from https://doi.org/10.1214/aos/1176347963 doi: 10.1214/aos/1176347963

Frisch, U. (1995). *Turbulence*. Cambridge University Press. Retrieved from https://

doi.org/10.1017/cbo9781139170666 doi: 10.1017/cbo9781139170666

Gingell, I., Schwartz, S. J., Burgess, D., Johlander, A., Russell, C. T., Burch, J. L., … Wilder, F. (2017, November). MMS observations and hybrid simulations of surface ripples at a marginally quasi-parallel shock. *Journal of Geophysical Research: Space Physics*, *122*(11). Retrieved from https://doi.org/10.1002/2017ja024538 doi: 10.1002/2017ja024538

Gingell, I., Schwartz, S. J., Eastwood, J. P., Burch, J. L., Ergun, R. E., Fuselier, S., … Wilder, F. (2019, February). Observations of magnetic reconnection in the transition region of quasi-parallel shocks. *Geophysical Research Letters*, *46*(3), 1177–1184. Retrieved from https://doi.org/10.1029/2018gl081804 doi: 10.1029/2018gl081804

Hollweg, J. V. (1999, July). Kinetic alfvén wave revisited. *Journal of Geophysical Research: Space Physics*, *104*(A7), 14811–14819. Retrieved from https://doi.org/10.1029/1998ja900132 doi: 10.1029/1998ja900132

Huang, S. Y., Hadid, L. Z., Sahraoui, F., Yuan, Z. G., & Deng, X. H. (2017, February). On the existence of the kolmogorov inertial range in the terrestrial magnetosheath turbulence. *The Astrophysical Journal*, *836*(1), L10. Retrieved from https://doi.org/10.3847/2041-8213/836/1/l10 doi: 10.3847/2041-8213/836/1/l10

Isenberg, P. A., & Hollweg, J. V. (1983). On the preferential acceleration and heating of solar wind heavy ions. *Journal of Geophysical Research*, *88*(A5), 3923. Retrieved from https://doi.org/10.1029/ja088ia05p03923 doi: 10.1029/ja088ia05p03923

Johlander, A., Schwartz, S., Vaivads, A., Khotyaintsev, Y. V., Gingell, I., Peng, I., … Burch, J. (2016, October). Rippled quasiperpendicular shock observed by the magnetospheric multiscale spacecraft. *Physical Review Letters*, *117*(16). Retrieved from https://doi.org/10.1103/physrevlett.117.165101 doi: 10.1103/physrevlett.117.165101

King, J. H. (2005). Solar wind spatial scales in and comparisons of hourly wind and ACE plasma and magnetic field data. *Journal of Geophysical Research*, *110*(A2). Retrieved from https://doi.org/10.1029/2004ja010649 doi: 10.1029/2004ja010649

Kiyani, K. H., Osman, K. T., & Chapman, S. C. (2015, May). Dissipation and heating in solar wind turbulence: from the macro to the micro and back again. *Philosophical Transactions of the Royal Society A: Mathematical, Physical and Engineering Sciences*, *373*(2041), 20140155. Retrieved from https://doi.org/10.1098/rsta.2014.0155 doi: 10.1098/rsta.2014.0155

Klimchuk, J. A. (2006, March). On solving the coronal heating problem. *Solar Physics*, *234*(1), 41–77. Retrieved from https://doi.org/10.1007/s11207-006-0055-z doi: 10.1007/s11207-006-0055-z

Kolmogorov, A. (1941, January). The Local Structure of Turbulence in Incompressible Viscous Fluid for Very Large Reynolds' Numbers. *Akademiia Nauk SSSR Doklady*, *30*, 301-305.

Lalti, A., Khotyaintsev, Y. V., Dimmock, A. P., Johlander, A., Graham, D. B., & Olshevsky, V. (2022, August). A database of MMS bow shock crossings compiled using machine learning. *Journal of Geophysical Research: Space Physics*, *127*(8). Retrieved from https://doi.org/10.1029/2022ja030454 doi: 10.1029/2022ja030454

Lepping, R. P., Acũna, M. H., Burlaga, L. F., Farrell, W. M., Slavin, J. A., Schatten, K. H., … Worley, E. M. (1995, February). The WIND magnetic field investigation. *Space Science Reviews*, *71*(1-4), 207–229. Retrieved from https://doi.org/10.1007/bf00751330 doi: 10.1007/bf00751330

Li, H., Jiang, W., Wang, C., Verscharen, D., Zeng, C., Russell, C. T., … Burch, J. L. (2020, July). Evolution of the earth's magnetosheath turbulence: A statistical study based on MMS observations. *The Astrophysical Journal*, *898*(2), L43. Retrieved from https://doi.org/10.3847/2041-8213/aba531 doi: 10.3847/2041-8213/aba531

Lindqvist, P.-A., Olsson, G., Torbert, R. B., King, B., Granoff, M., Rau, D., … Tucker, S. (2014, November). The spin-plane double probe electric field instrument for MMS. *Space Science Reviews*, *199*(1-4), 137–165. Retrieved from https://doi.org/10.1007/s11214-014-0116-9 doi: 10.1007/s11214-014-0116-9

Matsumoto, Y., Amano, T., Kato, T. N., & Hoshino, M. (2015, February). Stochastic electron acceleration during spontaneous turbulent reconnection in a strong shock wave. *Science*, *347*(6225), 974–978. Retrieved from https://doi.org/10.1126/science.1260168 doi: 10.1126/science.1260168

Matthaeus, W. H., Wan, M., Servidio, S., Greco, A., Osman, K. T., Oughton, S., & Dmitruk, P. (2015, May). Intermittency, nonlinear dynamics and dissipation in the solar wind and astrophysical plasmas. *Philosophical Transactions of the Royal Society A: Mathematical, Physical and Engineering Sciences*, *373*(2041), 20140154. Retrieved from https://doi.org/10.1098/rsta.2014.0154 doi: 10.1098/rsta.2014.0154

McComas, D., Bame, S., Barker, P., Feldman, W., Phillips, J., Riley, P., & Griffee, J. (1998).
Space Science Reviews, *86*(1/4), 563–612. Retrieved from https://doi.org/10.1023/a:1005040232597 doi: 10.1023/a:1005040232597

McKee, C. F., & Ostriker, E. C. (2007, September). Theory of star formation. *Annual Review of Astronomy and Astrophysics*, *45*(1), 565–687. Retrieved from https://doi.org/10.1146/annurev.astro.45.051806.110602 doi: 10.1146/annurev.astro.45.051806.110602

Milborrow, S., Hastie, T., & Tibshirani., R. (2011). earth: Multivariate adaptive regression splines [Computer software manual]. Retrieved from http://CRAN.R-project.org/package=earth (R package)

Ogilvie, K. W., Chornay, D. J., Fritzenreiter, R. J., Hunsaker, F., Keller, J., Lobell, J., … Gergin, E. (1995, February). SWE, a comprehensive plasma instrument for the WIND spacecraft. *Space Science Reviews*, *71*(1-4), 55–77. Retrieved from https://doi.org/10.1007/bf00751326 doi: 10.1007/bf00751326

Peredo, M., Slavin, J. A., Mazur, E., & Curtis, S. A. (1995). Three-dimensional position and shape of the bow shock and their variation with alfvénic, sonic and magnetosonic mach numbers and interplanetary magnetic field orientation. *Journal of Geophysical Research*, *100*(A5), 7907. Retrieved from https://doi.org/10.1029/94ja02545 doi: 10.1029/94ja02545

Phan, T. D., Eastwood, J. P., Shay, M. A., Drake, J. F., Sonnerup, B. U. O., Fujimoto, M., … Magnes, W. (2018, May). Electron magnetic reconnection without ion coupling in earth's turbulent magnetosheath. *Nature*, *557*(7704), 202–206. Retrieved from https://doi.org/10.1038/s41586-018-0091-5 doi: 10.1038/s41586-018-0091-5

Pollock, C., Moore, T., Jacques, A., Burch, J., Gliese, U., Saito, Y., … Zeuch, M. (2016, March). Fast plasma investigation for magnetospheric multiscale. *Space Science Reviews*, *199*(1-4), 331–406. Retrieved from https://doi.org/10.1007/s11214-016-0245-4 doi: 10.1007/s11214-016-0245-4

Ragot, B. R. (2022, March). Solar wind magnetic field correlation length: Correlation functions versus cross-field displacement diffusivity test. *The Astrophysical Journal*, *927*(2), 182. Retrieved from https://doi.org/10.3847/1538-4357/ac281b doi: 10.3847/1538-4357/ac281b

Russell, C. T., Anderson, B. J., Baumjohann, W., Bromund, K. R., Dearborn, D., Fischer, D., … Richter, I. (2014, August). The magnetospheric multiscale magnetometers. *Space Science Reviews*, *199*(1-4), 189–256. Retrieved from https://doi.org/10.1007/s11214-014-0057-3 doi: 10.1007/s11214-014-0057-3

Sahraoui, F., Goldstein, M. L., Belmont, G., Canu, P., & Rezeau, L. (2010, September). Three dimensional AnisotropickSpectra of turbulence at subproton scales in the solar wind. *Physical Review Letters*, *105*(13). Retrieved from https://doi.org/10.1103/physrevlett.105.131101 doi: 10.1103/physrevlett.105.131101

Sahraoui, F., Hadid, L., & Huang, S. (2020, February). Magnetohydrodynamic and kinetic scale turbulence in the near-earth space plasmas: a (short) biased review. *Reviews of Modern Plasma Physics*, *4*(1). Retrieved from https://doi.org/10.1007/s41614-020-0040-2 doi: 10.1007/s41614-020-0040-2

Smith, C., L'Heureux, J., Ness, N., Acuña, M., Burlaga, L., & Scheifele, J. (1998). *Space Science Reviews*, *86*(1/4), 613–632. Retrieved from https://doi.org/10.1023/a:1005092216668 doi: 10.1023/a:1005092216668

Stawarz, J. E., Eastwood, J. P., Phan, T. D., Gingell, I. L., Pyakurel, P. S., Shay, M. A., ... Contel, O. L. (2022, January). Turbulence-driven magnetic reconnection and the magnetic correlation length: Observations from magnetospheric multiscale in earth's magnetosheath. *Physics of Plasmas*, *29*(1), 012302. Retrieved from https://doi.org/10.1063/5.0071106 doi: 10.1063/5.0071106

Stawarz, J. E., Eastwood, J. P., Phan, T. D., Gingell, I. L., Shay, M. A., Burch, J. L., ... Franci, L. (2019, June). Properties of the turbulence associated with electron-only magnetic reconnection in earth's magnetosheath. *The Astrophysical Journal*, *877*(2), L37. Retrieved from https://doi.org/10.3847/2041-8213/ab21c8 doi: 10.3847/2041-8213/ab21c8

Torbert, R. B., Russell, C. T., Magnes, W., Ergun, R. E., Lindqvist, P.-A., LeContel, O., ... Lappalainen, K. (2014, November). The FIELDS instrument suite on MMS: Scientific objectives, measurements, and data products. *Space Science Reviews*, *199*(1-4), 105–135. Retrieved from https://doi.org/10.1007/s11214-014-0109-8 doi: 10.1007/s11214-014-0109-8

Wang, R., Lu, Q., Nakamura, R., Baumjohann, W., Russell, C. T., Burch, J. L., ... Gershman, D. (2017, October). Interaction of magnetic flux ropes via magnetic reconnection observed at the magnetopause. *Journal of Geophysical Research: Space Physics*, *122*(10), 10436–10447. Retrieved from https://doi.org/10.1002/2017ja024482 doi: 10.1002/2017ja024482

Yordanova, E., Vörös, Z., Raptis, S., & Karlsson, T. (2020, February). Current sheet statistics in the magnetosheath. *Frontiers in Astronomy and Space Sciences*, *7*. Retrieved from https://doi.org/10.3389/fspas.2020.00002 doi: 10.3389/fspas.2020.00002

Zhuravleva, I., Churazov, E., Schekochihin, A. A., Allen, S. W., Arévalo, P., Fabian, A. C., ... Werner, N. (2014, October). Turbulent heating in galaxy clusters brightest in x-rays. *Nature*, *515*(7525), 85–87. Retrieved from https://doi.org/10.1038/nature13830 doi: 10.1038/nature13830

JGR: Space Physics

Supporting Information for

Intermittency at Earth's bow shock: Measures of turbulence in quasi-parallel and quasi-perpendicular shocks

J. Plank[1], I. L. Gingell[1]

[1]School of Physics and Astronomy, University of Southampton, Southampton, UK

Contents of this file

Figures S1 to S8

Introduction

The supplementary material provided here includes tests of Taylor's hypothesis for events B and C, example plots of the magnetic spectrum for events A and D, and plots demonstrating the evolution of the spectral index fits, average spectral index, and kurtosis plots for events B and C. The methods used to create the figures are identical to those used for events A and D and are documented in the 'Results' section of the manuscript.

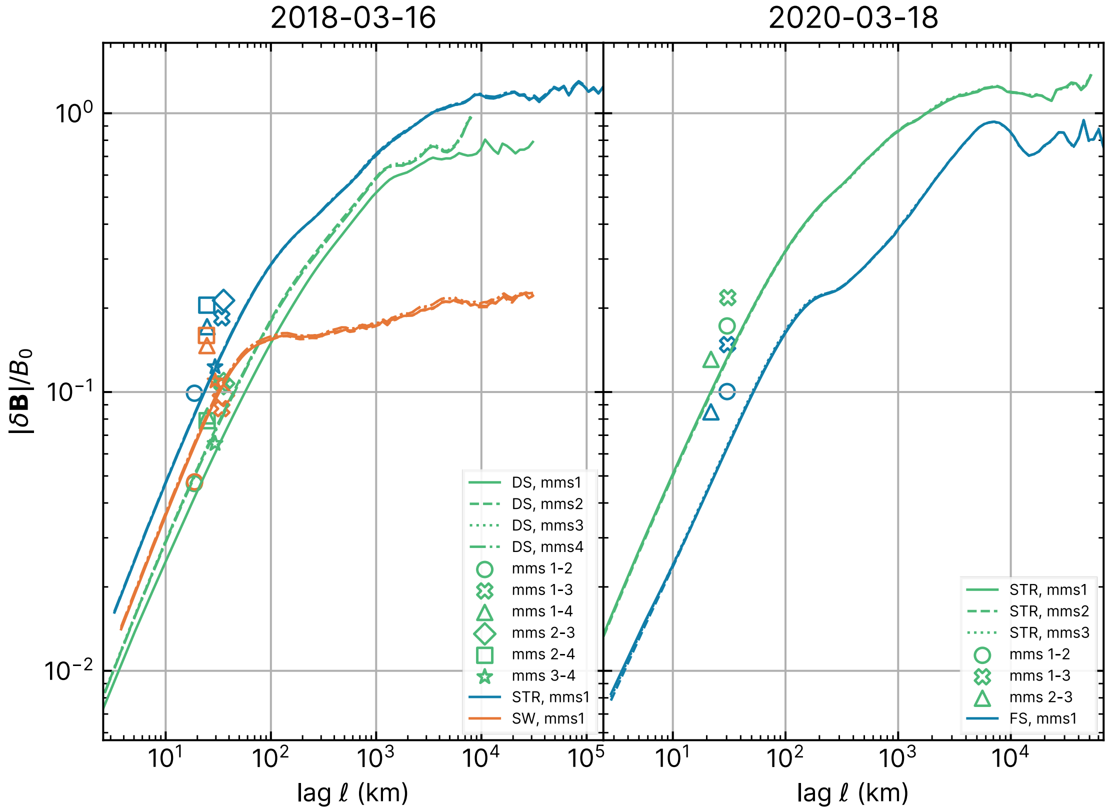

Figure S1: Magnetic fluctuation amplitude normalised to average field strength $|\delta\boldsymbol{B}|/B_0$ as a function of scale ℓ. *Left*: Event B, *right*: Event C. Fluctuation amplitude obtained using a single spacecraft and assuming Taylor's hypothesis is given by a line, solid for MMS 1, dashed for MMS 2, dotted for MMS 3, and dot-dashed for MMS 4. Colours represent the different regions of each event: Orange for solar wind (SW), blue for shock transition region (STR) or foreshock (FS), and green/red for the magnetosheath (MS). Measurements from the six spacecraft pairs, with ℓ equivalent to the separation scale, are shown by the following markers: Circle for MMS 1-2, cross for 1-3, triangle for 1-4, diamond for 2-3, square for 2-4, and star for 3-4.

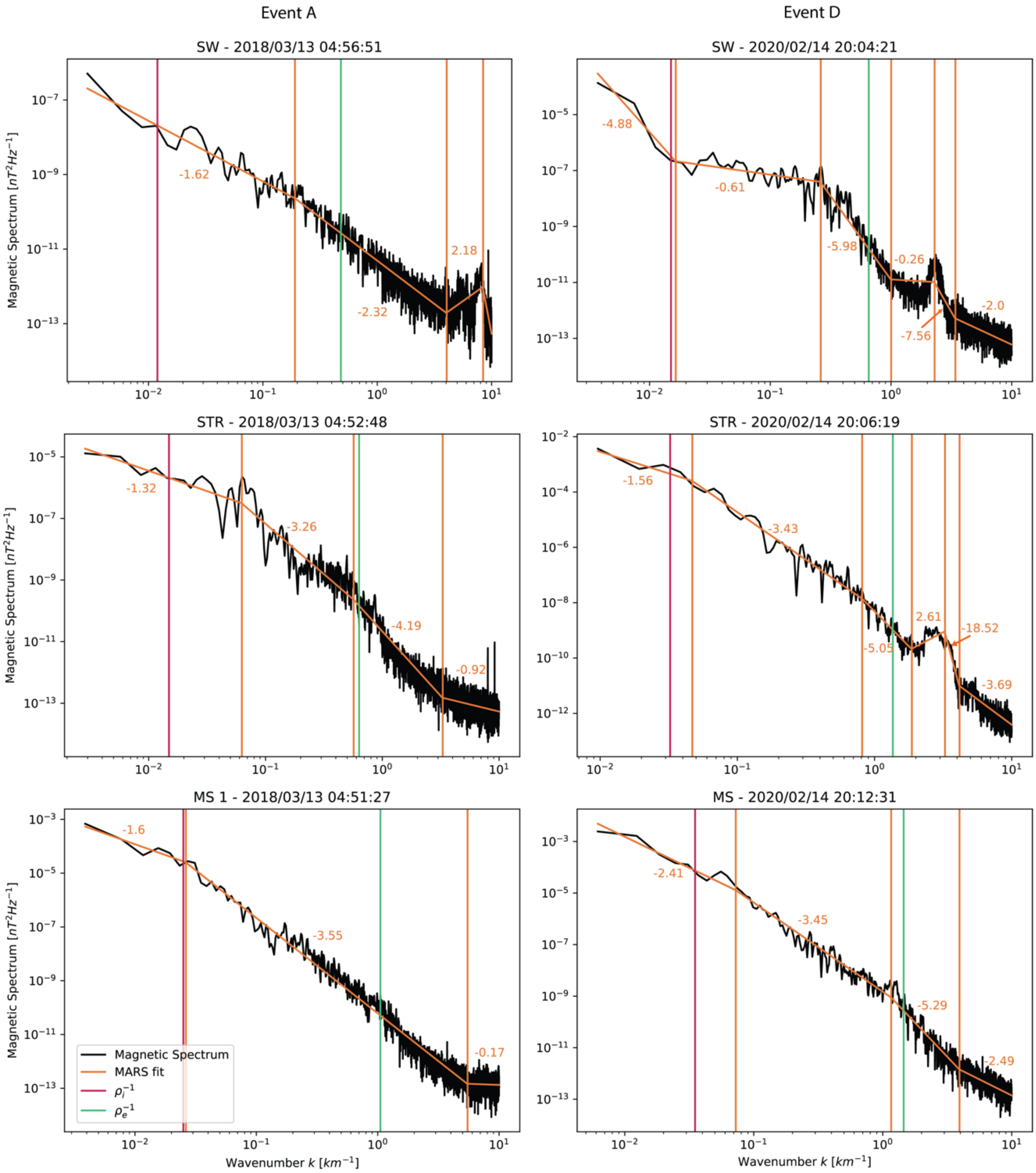

Figure S2: Example magnetic spectra, using the same format as figure 3 in the main manuscript. *Left column:* Event A. *Right column:* Event D. *Top row:* Windows (6s) in the solar wind (SW). *Middle Row:* Windows in the shock transition region (STR). *Bottom row:* Windows in the magnetosheath. The magnetic spectrum is shown in black. The MARS fit is shown in orange, with break points indicated by vertical orange lines at the break point location. For each slope the spectral index is noted in orange text. Ion and electron limits shown by red and green vertical lines, respectively.

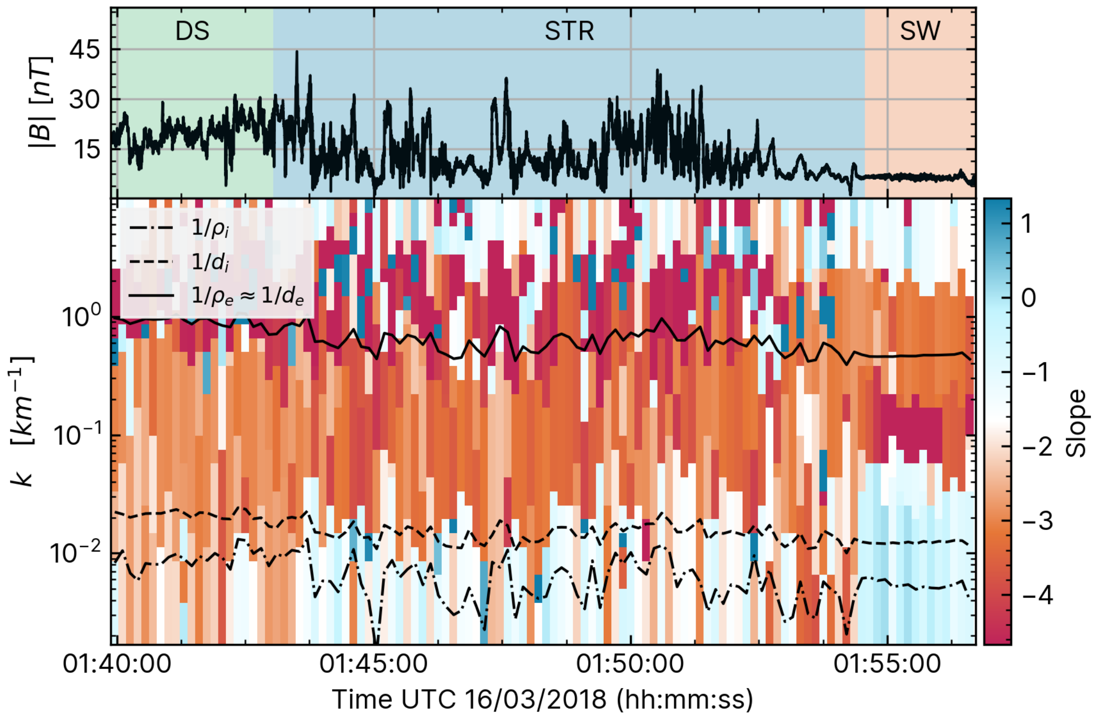

Figure S3. Evolution of spectral slopes as a function of time for event B. *Top:* Magnetic field strength, $\boldsymbol{B}$. Colours refer to downstream (DS) in green, shock transition region (STR) in blue and solar wind (SW) in orange. *Bottom:* Evolution of spectral indices from MARS fit. Note that this does not always split the spectrum into three regions. The colour represents the slope of the power-law fit. Red indicates steeper than $-5/3$, while blue is shallower than $-5/3$. Breakpoints are indicated by a change in colour. Electron scales, $\rho_e \approx d_e$ are shown as a solid black line, and ion scales d_i and ρ_i are dashed and dot-dashed black lines.

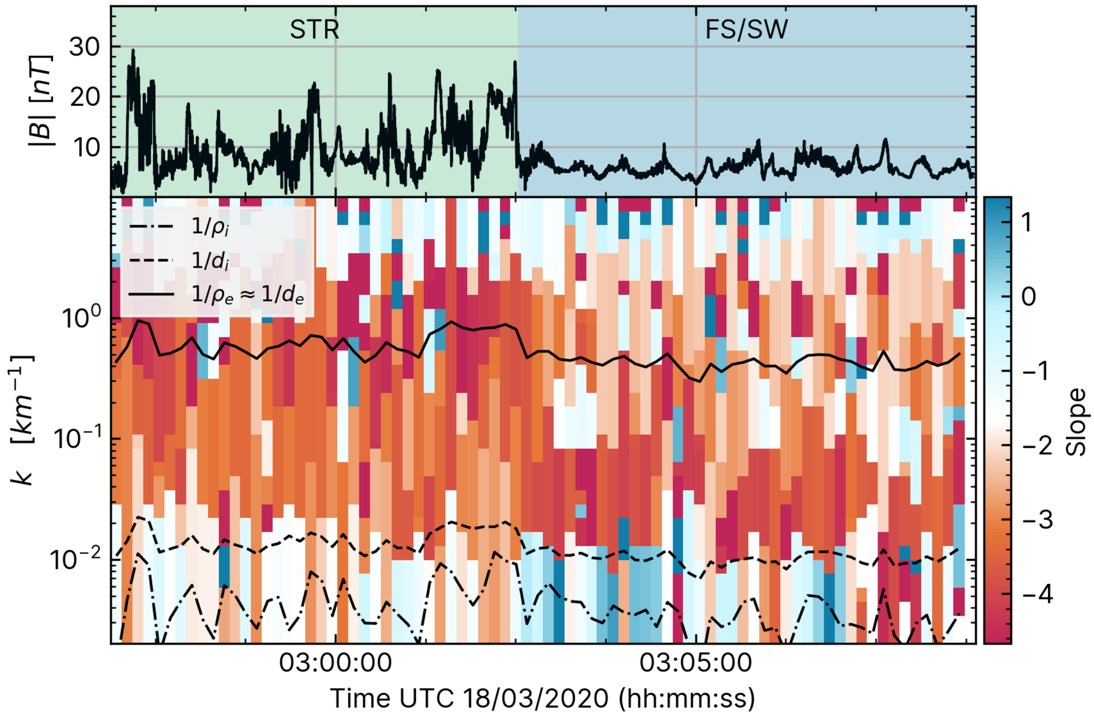

Figure S4. Evolution of spectral slopes as a function of time for event C. *Top:* Magnetic field strength, $\boldsymbol{B}$. Colours refer to shock transition region (STR) in green and foreshock/solar wind (FS/SW) in blue. *Bottom:* Evolution of spectral indices from MARS fit. Note that this does not always split the spectrum into three regions. The colour represents the slope of the power-law fit. Red indicates steeper than $-\mathbf{5/3}$, while blue is shallower than $-\mathbf{5/3}$. Breakpoints are indicated by a change in colour. Electron scales, $\boldsymbol{\rho_e} \approx \boldsymbol{d_e}$ are shown as a solid black line, and ion scales $\boldsymbol{d_i}$ and $\boldsymbol{\rho_i}$ are dashed and dot-dashed black lines.

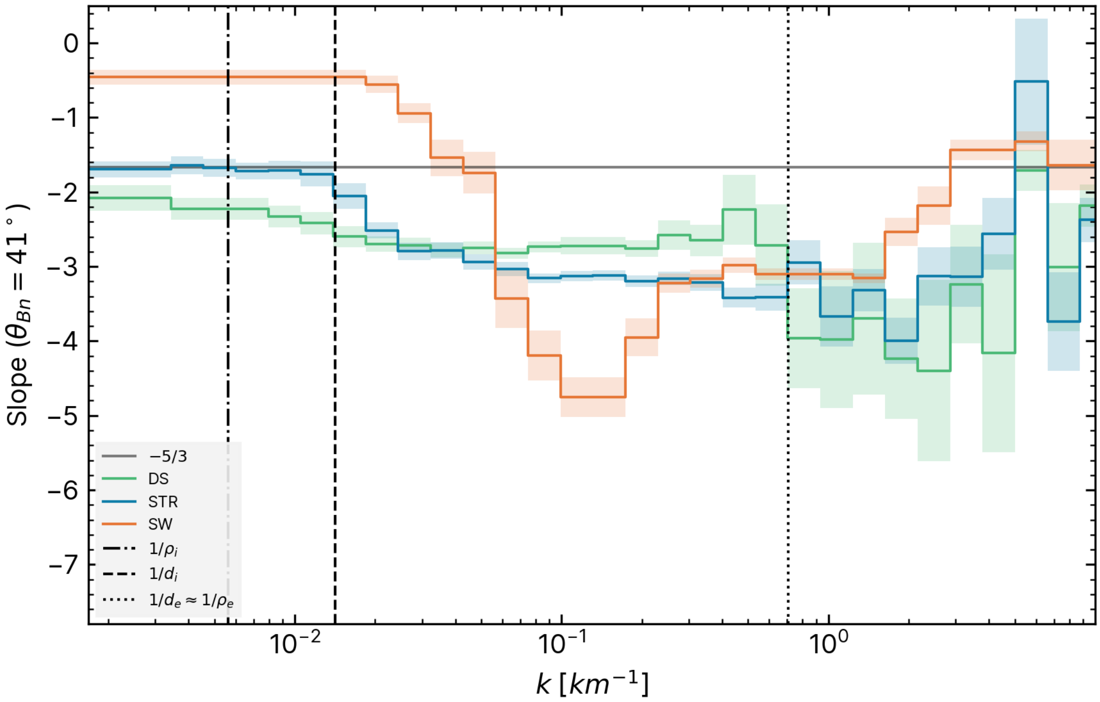

Figure S5. Average slope as a function of scale for event B. Each line represents a subsection of the entire interval. Downstream (DS) in green, shock transition region (STR) in blue, and solar wind (SW) in orange. The average ion gyroradius ρ_i and inertial length d_i are shown as dot-dashed and dashed lines respectively. The average electron gyroradius ρ_e and inertial length d_e are shown as a single dotted line. The Kolmogorov $-5/3$ slope is shown as a horizontal solid black line.

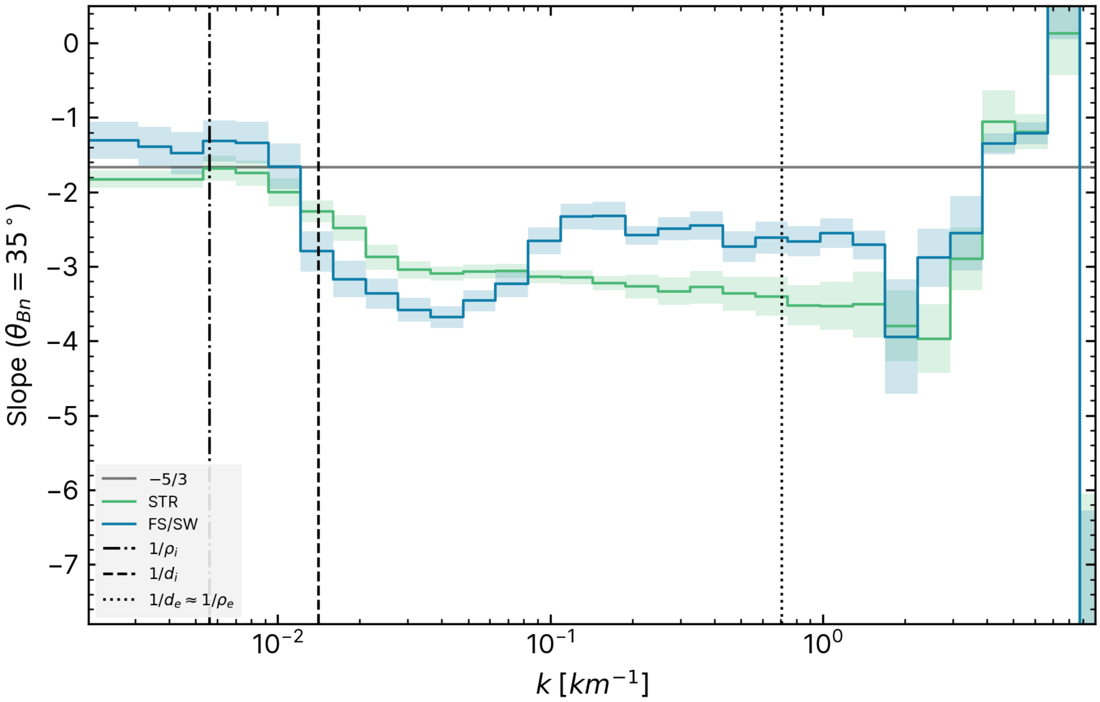

Figure S6. Average slope as a function of scale for event C. Each line represents a subsection of the entire interval. The shock transition region (STR) is shown in green, and the foreshock/solar wind (FS/SW) region is shown in blue. The average ion gyroradius ρ_i and inertial length d_i are shown as dot-dashed and dashed lines respectively. The average electron gyroradius ρ_e and inertial length d_e are shown as a single dotted line. The Kolmogorov $-5/3$ slope is shown as a horizontal solid black line.

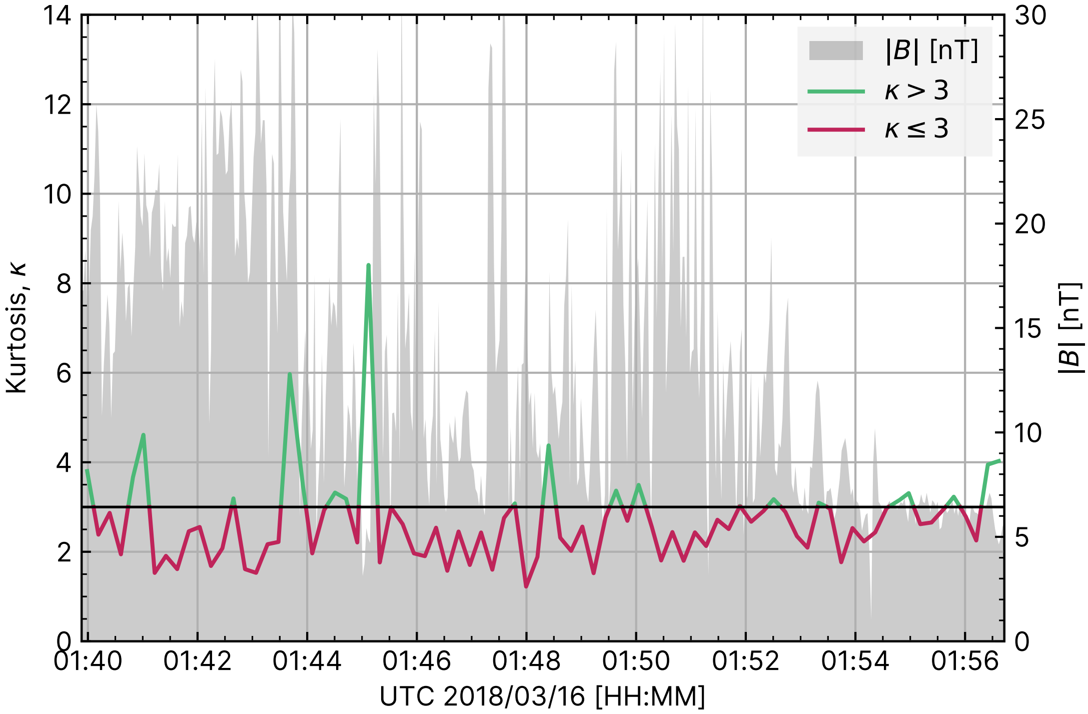

Figure S7. Kurtosis examined for event B. $\boldsymbol{\kappa} > \mathbf{3}$ is shown green, and $\boldsymbol{\kappa} \leq \mathbf{3}$ is red. A horizontal black line highlights $\boldsymbol{\kappa} = \mathbf{3}$. $|\boldsymbol{B}|$ is displayed for reference as a grey shaded background, with the vertical scale on the right.

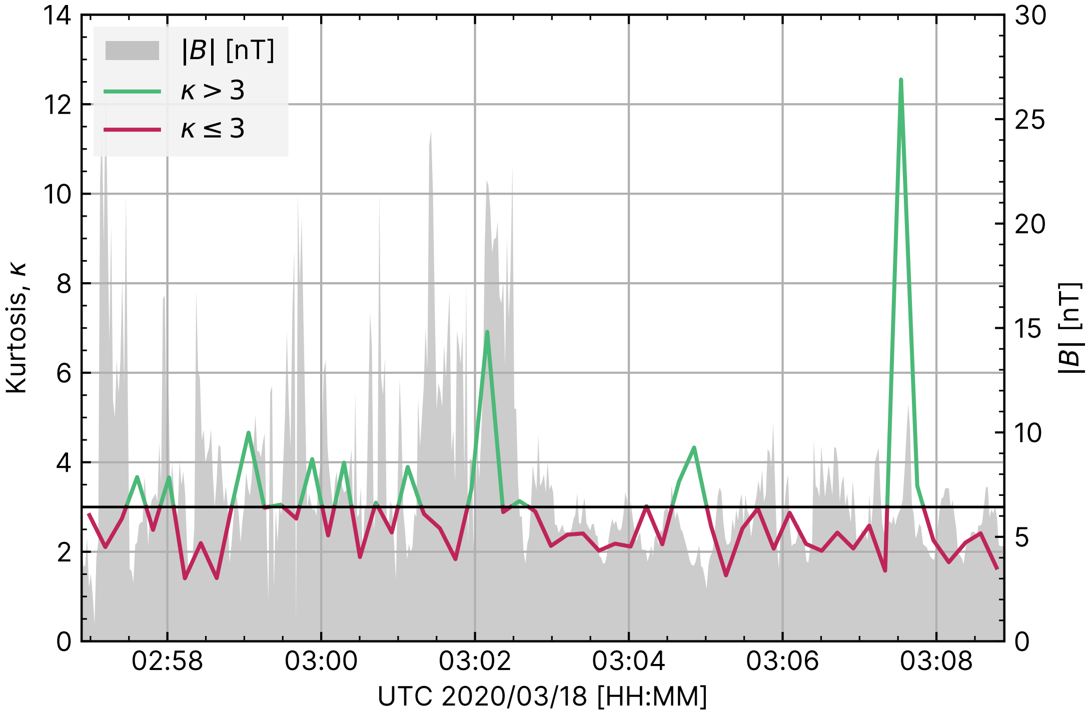

Figure S8. Kurtosis examined for event C. $\boldsymbol{\kappa > 3}$ is shown green, and $\boldsymbol{\kappa \leq 3}$ is red. A horizontal black line highlights $\boldsymbol{\kappa = 3}$. $|\boldsymbol{B}|$ is displayed for reference as a grey shaded background, with the vertical scale on the right.